Positron Plasma Control Techniques Applied to Studies of Cold Antihydrogen

冷たい反水素研究への陽電子プラズマ制御法の適用

Department of Physics, School of Science, University of Tokyo

Ryo Funakoshi
舩越 亮

December 2003

Abstract

In the year 2002, two experiments at CERN succeeded in producing cold antihydrogen atoms, first ATHENA and subsequently ATRAP. Following on these results, it is now feasible to use antihydrogen to study the properties of antimatter.

In the ATHENA experiment, the cold antihydrogen atoms are produced by mixing large amounts of antiprotons and positrons in a nested Penning trap. The complicated behaviors of the charged particles are controlled and monitored by plasma manipulation techniques. The antihydrogen events are studied using position sensitive detectors and the evidence of production of antihydrogen atoms is separated out with the help of analysis software.

This thesis covers the first production of cold antihydrogen in the first section as well as the further studies of cold antihydrogen performed by using the plasma control techniques in the second section.

Contents

List of Figures

List of Tables

Chapter 1

Introduction

Antihydrogen is the simplest atom, composed only of an antiproton and a positron. Antimatter should have completely the same characteristics as matter, with an equal mass, an equal lifetime, and an equal and opposite charge (Fig. 1.1). The existence of antimatter was first predicted by Dirac in 1930 and subsequently Anderson observed the first positron in 1932 in a cosmic shower. It was the first experiment that succeeded in conclusively showing evidence of antimatter in the world. Since then physicists made many experiments using antimatter and have done important measurements that contributed to the advance of physics.

In this section the history and the motivation for making antihydrogen atom are described.

1.1 Motivation and History

1.1.1 CPT Theorem

The production of cold antihydrogen is required in order for it to be useful for a wide variety of areas from fundamental physics to the industrial world, and one of the strongest motivations is that antihydrogen is expected to be useful for very high precision test of CPT. The CPT theorem plays an important role in elementary particle physics and tells us that physics rules are unchanged by the application of operation of CPT, which is the combined operations of charge conjugation (C), parity reversal (P) and time reversal (T), with assumptions of quantum field theory, Lorenz invariance and unitarity. As

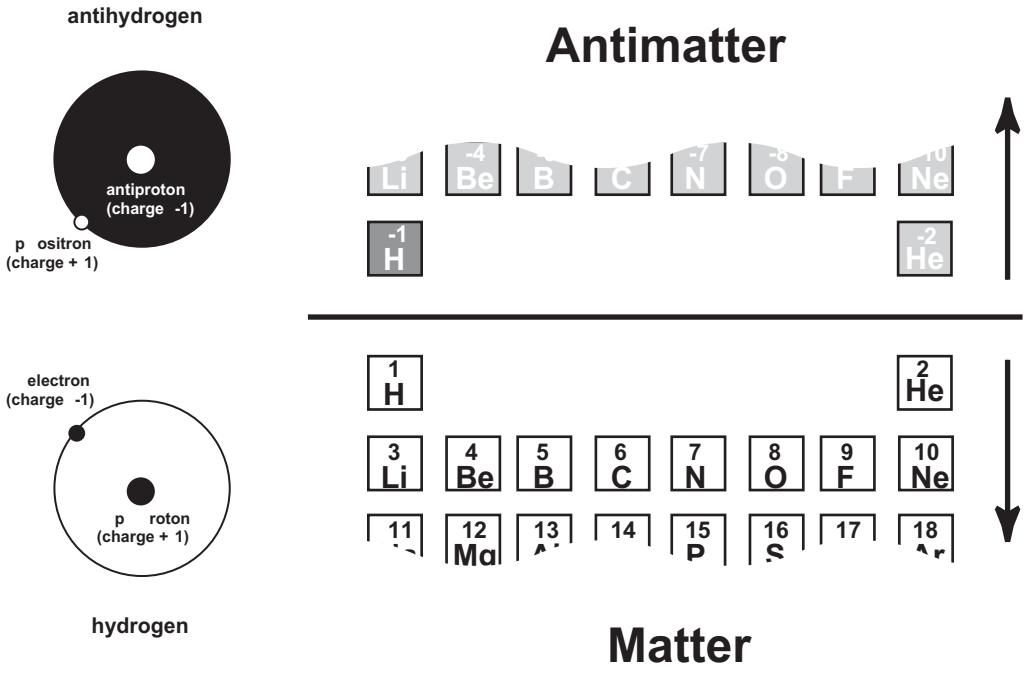

Figure 1.1: The periodic table of the elements. The characteristics of antimatter are almost same as that of matter, just like the world reflected by a mirror. Antihydrogen (composed of an antiproton and a positron) corresponds to Hydrogen, and its atomic number may be defined as '-1 '.

a consequence, this theorem gives some indications about the relationships between particles and antiparticles. They should have equal masses and lifetimes, and equal and opposite charges. Search for differences of these parameters between particles and their antiparticles leads to the direct tests of CPT.

1.1.2 Spectroscopy with Antihydrogen

P (and C) violation was observed in the year of 1957 and CP violation was observed in 1964. Although CPT is considered to be conserved, to check for CPT invariance is still an important task for physics. So far the (direct) highest precision test of CPT has been achieved to 10^{-9} by comparing the mass differences between an electron and a positron [4].

The antihydrogen atom is expected to be one of the most powerful tools for high precision tests of CPT. Since the antihydrogen atom is a bound state composed of an antiproton and a positron, the energy levels can be measured by a laser system. In fact, the 1 s - 2 s energy level difference of the Hydrogen atom, the configuration of which is the same as of the antihydrogen atom, can be observed to precision of 10^{-14} (Fig. 1.2 and [1]). Laser spectroscopy applied to the antihydrogen atom is expected to yield similar results, and hence well serves as the most stringent direct test of CPT.

1.1.3 High Energy Antihydrogen atoms

The first antihydrogen atoms were produced at relativistic energies in 1995 at the Low Energy Antiproton Ring (LEAR) at CERN [2] and later (1997) at Fermilab [3]. In the LEAR experiment, nine atoms were produced in collisions between antiprotons and xenon atoms over a period of three weeks. 2 GeV/c antiprotons passing through a xenon gas jet target created electron-positron pairs, and occasionally, an antiproton captured one of the positrons and recombined to form an antihydrogen atom:

$$\bar{\mathrm{p}} + \mathrm{Z} \rightarrow \bar{\mathrm{H}} + \mathrm{Z} + \mathrm{e}^{-}.$$

Each of the produced atoms remained in existence for about 40 ns, traveled at nearly at the speed of light and then annihilated with matter. Because of the high velocity (hence short lifetime), this production method is not easily applicable in a practical way to high precision studies of antihydrogen properties. Production of cold antihydrogen is therefore awaited.

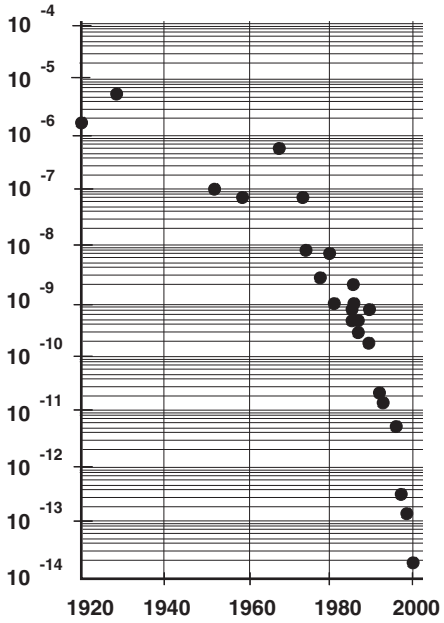

Figure 1.2: High precision measurements achieved by laser spectroscopy. The graph shows the precision of the measured energy level difference of 1 s - 2 s transitions of hydrogen atom versus the year of the experiment.

1.2 Antiproton Decelerator (AD)

After the shut down of LEAR in 1996 a new slow antiproton source was required by low energy antimatter physicists and the building of a new facility, Antiproton Decelerator (AD), started at CERN in 1999.

The AD, commissioned in 1999, is the only facility in the world that provides the low energy antiproton beam (Fig. 1.3). Antiprotons are created in the collisions of 26 GeV protons on an iridium target; protons are provided by proton synchrotron (PS) accelerator located upstream of the AD. Antiprotons are produced at about 3 GeV with a large energy as well as angular spread.

The bending magnets make them stay on the right track, while they begin to go around in the ring.

One deceleration cycle of the AD is shown in Fig. 1.4. AD cycles consists of cooling and deceleration sections. The high energy antiprotons injected from upstream are cooled down, i.e., energy and angular spreads are reduced, by applying the techniques of stochastic cooling and electron cooling. Finally the antiprotons are decelerated to 5.3 MeV and are ejected from the ring in a short (~ 100 ns) bunch. Each bunch contains 2×10^7 antiprotons, and the cycle is repeated every ~ 85 s

1.3 The ATHENA project

The following three projects are installed in the AD hall:

ATHENA Antihydrogen Production and Precision Experiments

ATRAP Cold Antihydrogen for Precise Laser Spectroscopy

ASACUSA Atomic Spectroscopy and Collisions using Slow Antiprotons

This thesis mentions the ATHENA experiment which the author joined. The goals of the ATHENA experiment are, 1) production of cold antihydrogen atoms and 2) laser spectroscopy applied to antihydrogen atoms for high precision tests of CPT.

This thesis is organized as follows: In Chapter 2, the ATHENA apparatus is described in detail. The first production and detection of cold antihydrogen

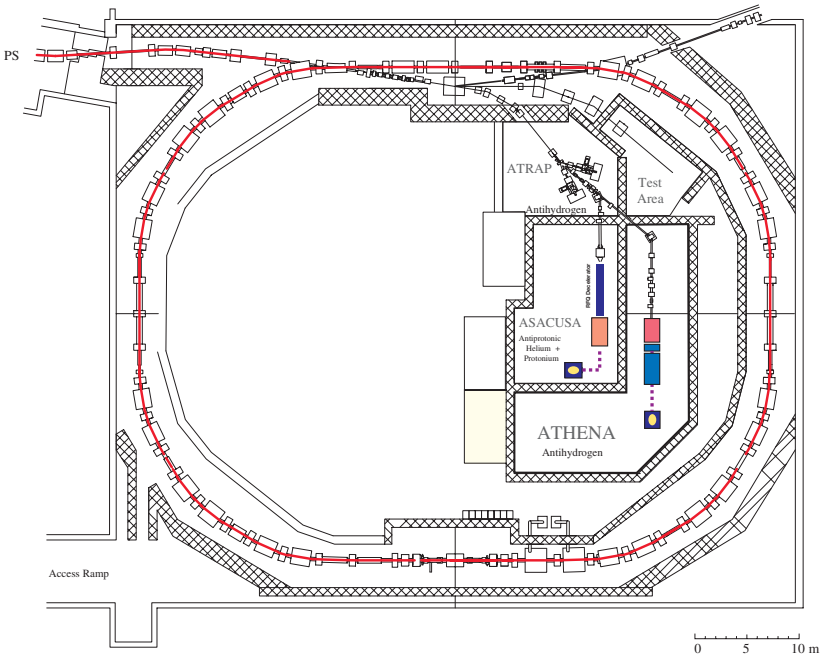

Figure 1.3: The figure of the antiproton decelerator (AD) facility. The high energy antiprotons injected from the upstream production target are decelerated and cooled down in 85 s, and the low energy pulsed beam is shared by three experiments.

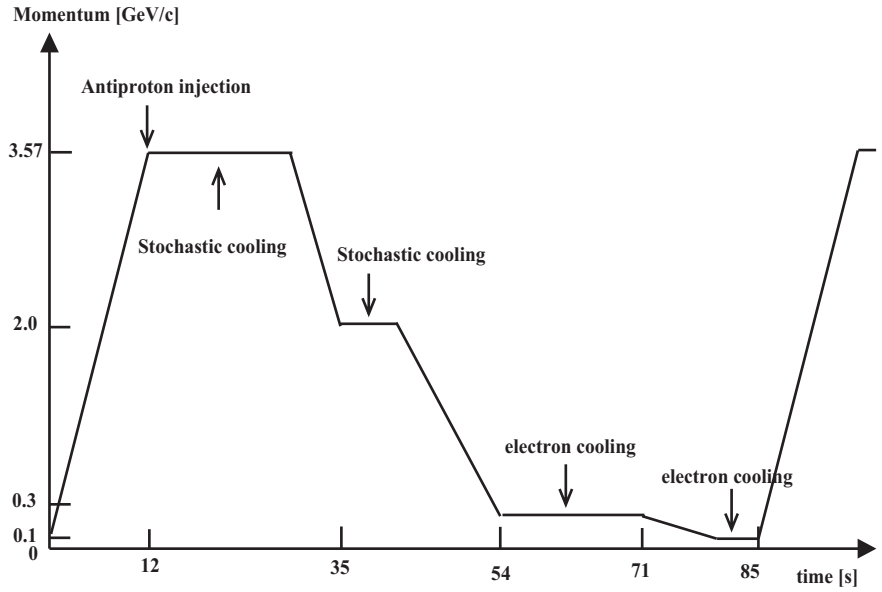

Figure 1.4: Each AD cycle consists of cooling and deceleration sections. The high energy antiprotons injected form the upstream are cooled down by applying the techniques of stochastic cooling and electron cooling, and the beam is decelerated to 5.3 MeV in less than 85 s.

is presented in Chapter 3. Further studies of cold antihydrogen performed by using plasma control techniques is described in Chapter 4, and summary is given in Chapter 5.

The author's main contribution is the development of the plasma manipulation techniques in antihydrogen production experiment. The plasma manipulation techniques for positrons have realized the flexible control and be the useful monitoring system when positron and antiprotons are mixed in the trap system as described in Chapter 2 and 3. And this technique is also applicable to further studies of produced antihydrogen, which will lead us to the future experiments. As one of the cases, the density dependence of the antihydrogen production has been achieved with the help of plasma techniques in Chapter 5. In the ATHENA experiment, the antihydrogen is expected to be produced mainly from radiative process and three-body process. These two processes make different distribution of the quantum stated of the captured positron and also have different dependence on the positron density and temperature. Therefore the information of the formation mechanism and the state distribution can be obtained by the study of the density dependence of the antihydrogen production. Well understanding of the state distribution and the control technique of the formation process, in order to prepare the required state, will be helpful to the laser spectroscopy experiment. Plasma technique parameters were optimized to inserted this technique to the ATHENA antihydrogen production cycle, and the density dependence has been studied for the first time.

Chapter 2

The ATHENA Experiment

The ATHENA apparatus, which is designed for production of cold antihydrogen, is explained in this chapter. First, the basic philosophy is discussed in order to clarify the required experimental condition for antihydrogen production. Details of each part of the apparatus are then described.

2.1 Experimental Approach

The ATHENA scheme for producing cold antihydrogen atoms are shown in Fig 2.1. Low energy antiprotons from AD are captured, cooled down and trapped. Positrons from the radioactive source are also cooled down, and accumulated. By mixing two species, cold antihydrogen atoms are expected to be produced.

In producing antihydrogen, the following two mechanisms are important; the spontaneous radiative recombination of antiprotons and positrons ($\bar{\mathrm{p}} + \mathrm{e}^+ \rightarrow \bar{\mathrm{H}} + \gamma$), and the three-body recombination ($\bar{\mathrm{p}} + \mathrm{e}^+ + \mathrm{e}^+ \rightarrow \bar{\mathrm{H}} + \mathrm{e}^+$). In both of these processes, the antihydrogen formation rates increase towards low temperature as $T^{-1/2}$ for the radiative, and as $T^{-9/2}$ for the three-body, and hence, it is important to prepare 'cold' antiprotons and positrons. Also important is to achieve high density of particles. For example, the spontaneous formation rate is predicted to be [13]

$$R = N_{\bar{p}} 1.92 \times 10^{-13} n_{e^+} (k_B T)^{-1/2} (1.73 - \frac{1}{2} \log(k_B T)) \sec^{-1}, \qquad (2.1)$$

where $N_{\bar{p}}$ is the number of antiprotons, n_{e^+} is the positron density (cm^{-3}), k_B is the Boltzmann constant and T is the temperature(K). For example,

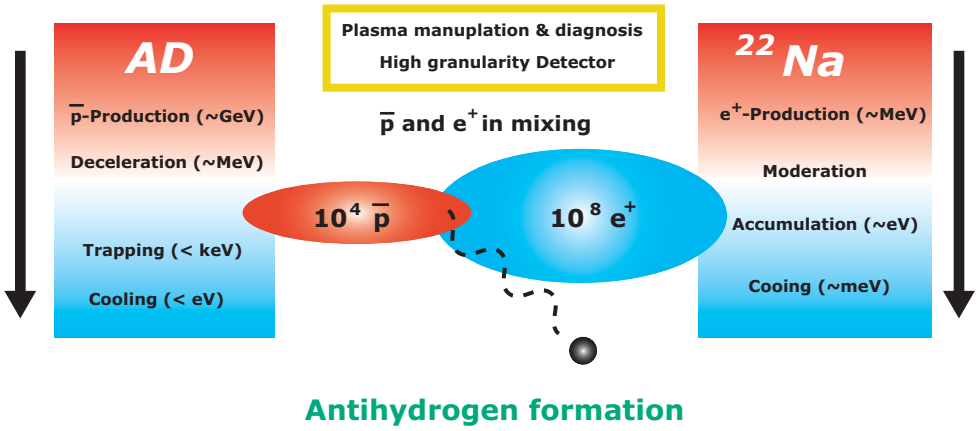

Figure 2.1: The basic scheme of production of cold antihydrogen. Low energy antiprotons from AD are captured, cooled down and trapped. Positrons from the radioactive source are also cooled down, and accumulated. By mixing these two low energy species, the cold antihydrogen atoms are produced.

with $N_{\bar{p}} = 10^4$, $n_{e^+} = 10^8\,\mathrm{cm}^{-3}$ and $T = 15\,\mathrm{K}$ (achievable in ATHENA), R is $27\,\mathrm{s}^{-1}$.

It follows that we need to merge large number of antiprotons and positrons within the small region at the low temperature for production of antihydrogen in either way.

2.2 ATHENA Apparatus

The overview of ATHENA is shown in Fig. 2.2. The apparatus is composed of 1) antiproton catching trap, 2) mixing trap, 3) positron accumulator, and 4) antihydrogen detector. The catching trap and the mixing trap are in 3 T superconducting solenoid, and are kept at 15 K. The antihydrogen detector surrounds the mixing trap.

2.2.1 Superconducting Solenoid Magnet

The magnet used in ATHENA experiment is a superconducting solenoid with a 150 mm diameter and a homogeneous field region of 1 m length. All the data presented in this thesis were taken with a field strength of 3 T.

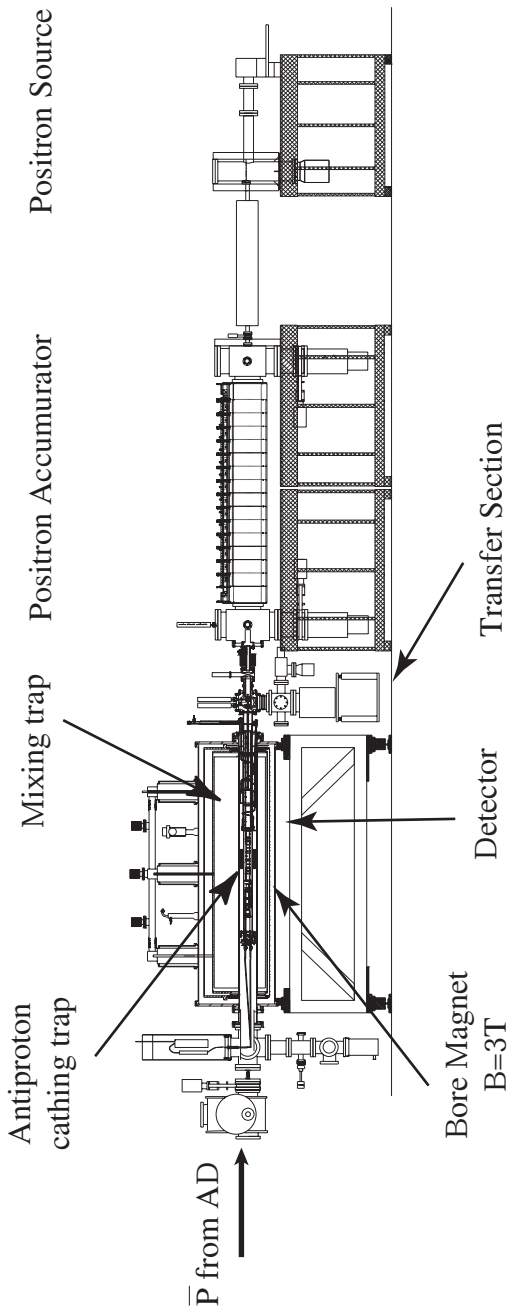

Figure 2.2: Overview of the ATHENA apparatus for the production of antihydrogen. The instruments are composed of 1) antiproton catching trap, 2) mixing trap, 3) positron accumulator and 4) antihydrogen detector.

2.2.2 The Vacuum and Cooling System

There are two independent vacuum volumes in the inner-bore of the solenoid. The inner-most volume is called 'cold nose' , cooled down to some 15 K by using a constant-flow helium cryostat. The catching trap and the mixing trap are in this volume. The pressure can be measured only outside of the cold region, where 10^{-11} mbar is routinely achieved (inside of the cold nose expected to be much less). Such high vacuum is required in order to avoid antiproton loss due to annihilation with residual gas.

The cold nose is surrounded by the 'outer vacuum', in which antihydrogen detectors are installed. The temperature is kept at ~ 130 K.

These two parts are completely separated from each other from the view of both thermal and vacuum conditions by the thermal shield (consisted of aluminum and Kapton) and the wall of the cold nose.

2.2.3 Penning trap system

The ATHENA experiment uses two Penning trap systems, one is for antiproton catching and the other is for positron and antiproton mixing for producing antihydrogen [47]. Each trap is composed of a sequence of cylindrical electrodes having 1.25 cm inner radius and various length to perform the flexible operation. Proceeding from the antiproton beam entrance and moving toward the positron accumulator, first 12 electrodes are used for antiproton cooling, catching and accumulation (the catching trap). The following groups are referred as the mixing trap, where the antiprotons from the catching trap and the positrons from the positron accumulator are merged. The rest part of the electrodes are used for positron transfer and recapturing procedure in the main magnet.

Antiproton catching trap

The catching trap shown in Fig. 2.3 contains 12 cylindrical electrodes. Two end-cap electrodes are used to apply the high voltage for catching antiprotons and the central 10 electrodes are used for confinement of cold antiprotons. Seven electrodes at the center parts are specially designed to make a harmonic potential for cooling and trapping of antiprotons.

The procedure of catching and cooling of antiprotons is shown in Fig. 2.4. The potential of the entrance electrode (HVL) at the end of the catching trap

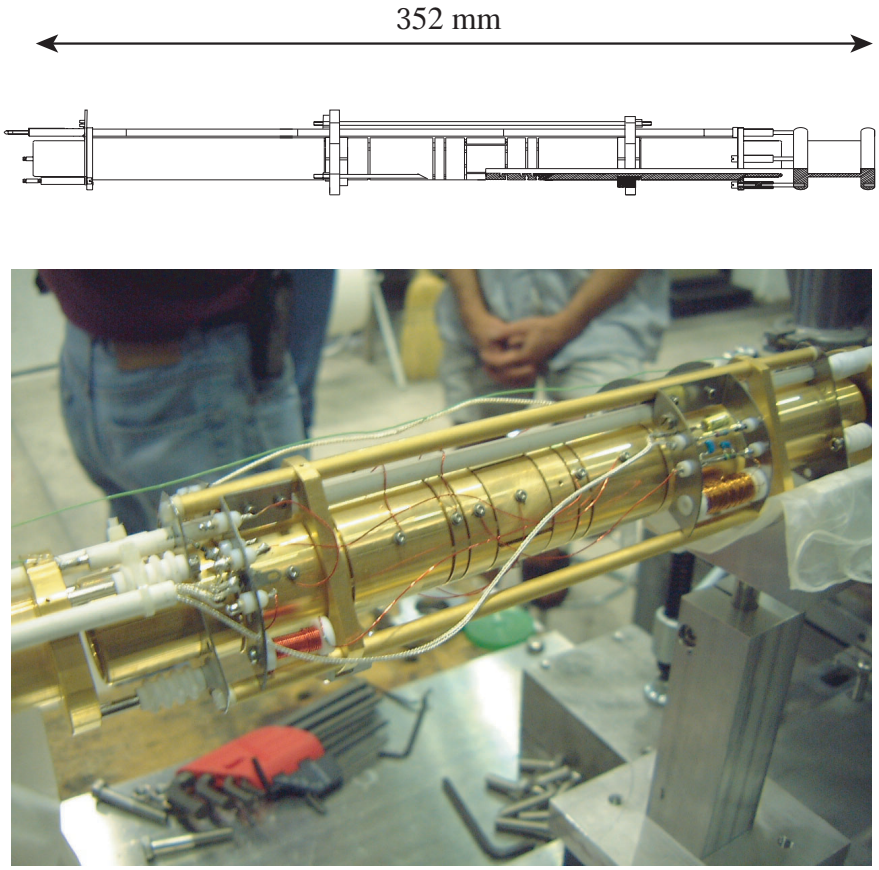

Figure 2.3: The antiproton catching trap. The trap consists of 12 cylindrical electrodes and is designed to allow the application of up to 15 kV to the end-cup electrodes.

is initially set to 0 V and opposite side (HVR) set to $V_{\rm HV}$.

The antiproton kinetic energy is degraded by 25 μm of stainless steel, located 10 cm upstream of the catching trap, and by 130 μm of aluminum on the entrance electrode. Only antiprotons with the energy lower than e$V_{\rm HV}$ are reflected by the potential on HVR. The voltage $V_{\rm HV}$ is applied to HVL before they pass HVL on their way back, and they are captured between HVL and HVR.

The timing to 'close the trap door' was experimentally optimized by maximizing the number of trapped antiprotons (see Fig. 2.6). The trapped antiprotons were released by lowering the entrance voltage and allowed them to annihilate on the degrader. The number of captured antiprotons is measured by the scintillators, which are located outside the main magnet (called external beam detectors) as skeched in Fig.2.5. Fig. 2.6**a** shows how the number of trapped antiprotons increases with the applied voltage $V_{\rm HV}$. Typical number of trapped antiprotons with 5 kV potential is around 10^4 at one AD shot (2×10^7 antiprotons are contained). Fig. 2.6**b** shows closing time dependence of the number of trapped antiprotons. The optimum closing time is $500 - 700$ ns.

Antiproton Cooling Captured antiprotons are cooled down by energy loss via Coulomb collision with preloaded electrons.

The cooling process is usually described by the differential equations [23]

$$\begin{aligned} \frac{dT_{\bar{p}}}{dt} &= -\frac{(T_{\bar{p}} - T_{e^-})}{\tau_{c\bar{p}}}, \\ \frac{dT_{e^-}}{dt} &= \frac{1}{\tau_{ce^-}}(T_{\bar{p}} - T_{e^-}) - \frac{(T_{e^-} - T_t)}{\tau_{e^-}}, \end{aligned}$$

where T_{e^-} and $T_{\bar{p}}$ are the electron and antiproton temperatures, T_t is the environment temperature, n_{e^-} and $n_{\bar{p}}$ are the electron and antiproton densities. The time constant τ_{e^-} represents the synchrotron cooling time of electrons, which is experimentally determined as about 0.5 s in a magnetic field of 3 T. The cooling (or heating) due to Coulomb collision is represented by τ_c given by,

$$\tau_{c\bar{p}(e^-)} = \frac{3 m_{\bar{p}} m_{e^-} c^3}{8(2\pi)^{1/2} n_{e^-(\bar{p})} e^4 \ln \Lambda_{\bar{p}(e^-)}} \left(\frac{k_B T_{\bar{p}}}{m_{\bar{p}} c^2} + \frac{k_B T_{e^-}}{m_{e^-} c^2} \right)^{3/2}.$$

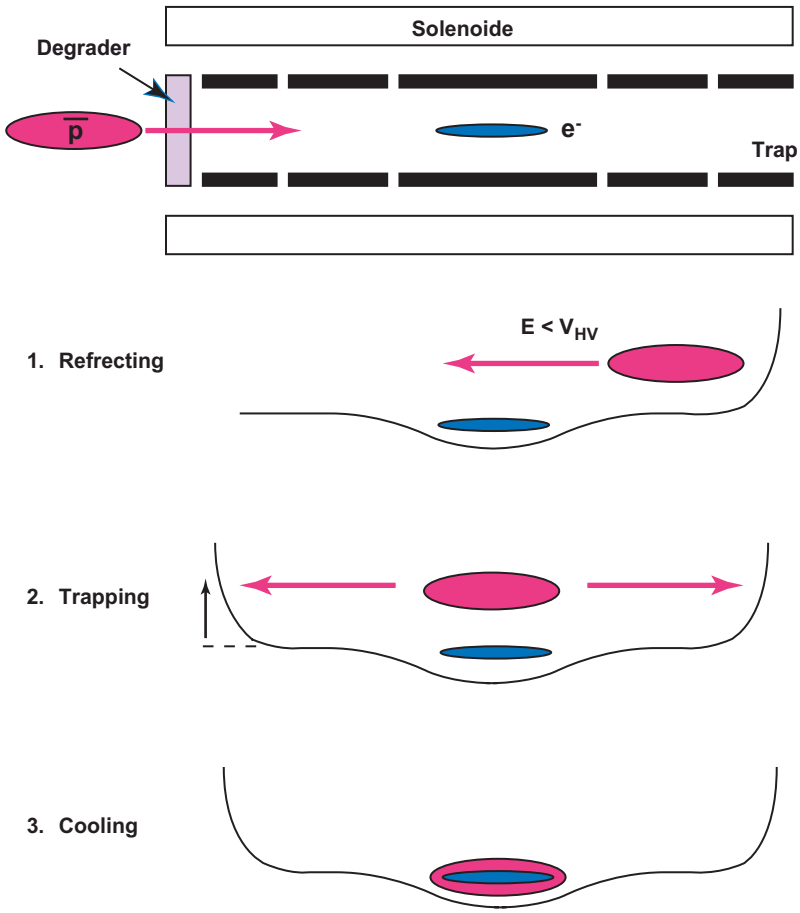

Figure 2.4: The schematic picture of electron cooling applied to the antiprotons. **1** The high energy antiprotons are reflected by the high voltage wall, which is set at the end cap of the antiproton catching trap (HVR). **2** The high voltage at the entrance side is raised before the escape of bounced antiprotons. **3** The trapped antiprotons are cooled down by the collision with the pre-loaded electrons.

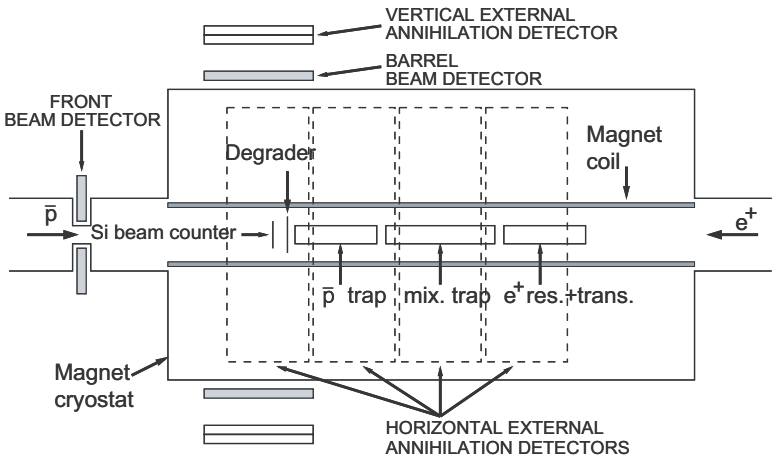

Figure 2.5: The antiproton beam line and the external beam detector position (not to scale). Figures are taken from [11].

Here $m_{\bar{p}}$ and m_{e^+} are the antiproton and electron masses, e is their electrical charge and Λ is given by

$$\Lambda_{\bar{p}(e^-)} = \frac{4\pi\epsilon_0}{n_{e^-(\bar{p})}} \left(\frac{k_B T_{e^-(\bar{p})}}{e^2} \right)^{3/2}.$$

The solution of these equations shows that 10^4 antiprotons with the energy of the keV can be cooled down to a few eV within 1 s, if they completely overlap with an electron cloud of $n_{e^-} = 10^8\,\mathrm{cm}^{-3}$.

Electrons are emitted from a barium oxide disc cathode (Kimball Physics Inc.) which is mounted on a movable stick placed at the positron transfer region (see Sec. 2.2.4). Electrons are loaded into the trap region before antiproton injection from AD.

The cooling procedure is studied by two different kinds of the dumping steps; the 'hot antiprotons' from the high voltage dump and 'cold antiprotons' from the internal shallow well where they are cooled by electrons. Fig. 2.7 shows a typical time distribution of hot and cold antiproton annihilations on the entrance degrader. The potential well is first lowered from 5 kV to 40 V with a time constant of about 20 ms to release the energetic antiprotons (marked as HV dump in Fig. 2.7) and then from 40 V to 0 V in about 1 s to dump the slower antiprotons which are cooled via interaction with the

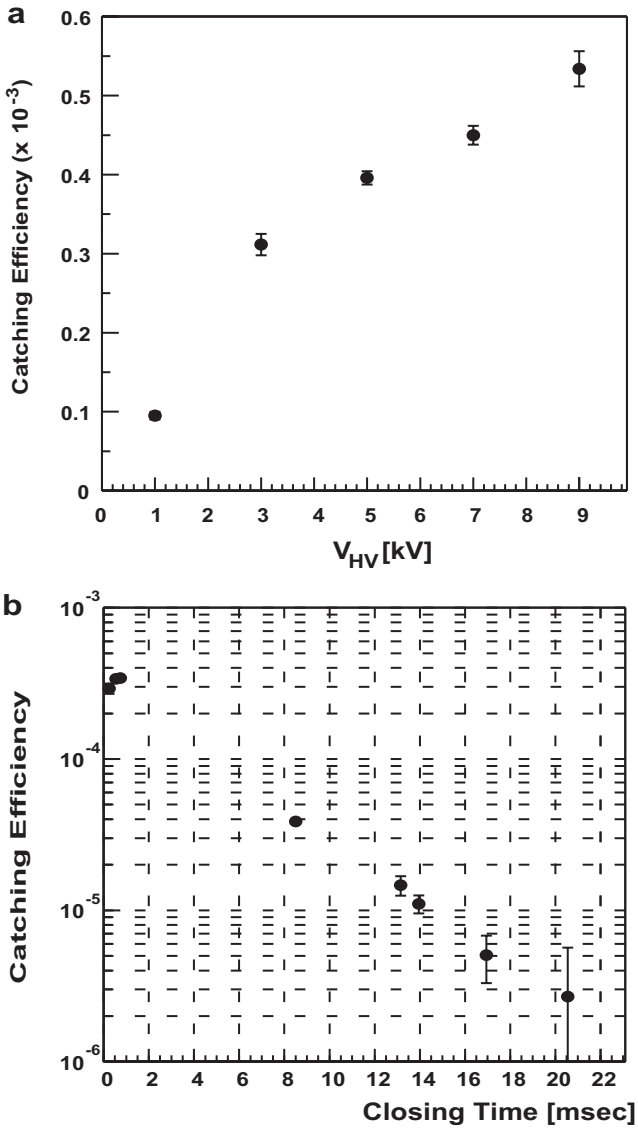

Figure 2.6: The characteristic dependence of antiproton catching efficeinecy for trap parameters. **a,** Dependence of the catching efficiency on the applied high voltage, VHV. The antiprotons were released from the trap 1 s after capturing. The numbers of captured antiprotons are normalized to the beam intensity measured by external beam detectors. **b,** Dependence of the catching efficeinecy on the trap closing time delay. Figures are taken from [11].

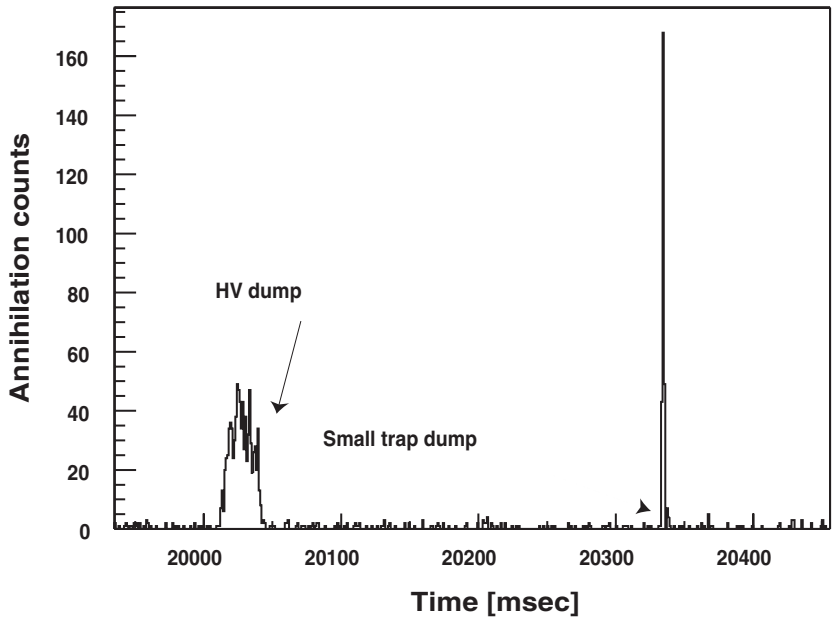

Figure 2.7: A typical antiproton annihilation time spectrum measured by the external annihilation detector (see text). The clock is started at injection of the antiproton beam into the trap. The figure is taken from [11].

preloaded electrons (marked as slow trap dump in Fig. 2.7). Fig. 2.8**a** shows the fraction of hot and cold antiprotons as a function of interaction time. Almost all of the electrons can be cooled in about 60 s cooling time. In this way, several thousands of cold antiprotons are trapped in the central region. The space-charge due to the trapped antiprotons is not so large as compared with the trapping potential, thus several AD shots can be stacked within the trap keeping the same electron cloud. With this antiproton stacking scheme, the number of cold antiprotons linearly increases with the number of AD shots in the catching trap (Fig. 2.8**b**).

Antiproton Storage Time Antiproton storage time is influenced by the presence of electrons used in the cooling procedure. At the end of the electron cooling, the antiprotons and electrons share the same volume, but the electrons can be selectively removed from the trap well by applying a short electric pulse of about 100 ns, which do no affect antiprotons with heavier mass. Fig. 2.9 shows the antiproton lifetime with or without electrons af-

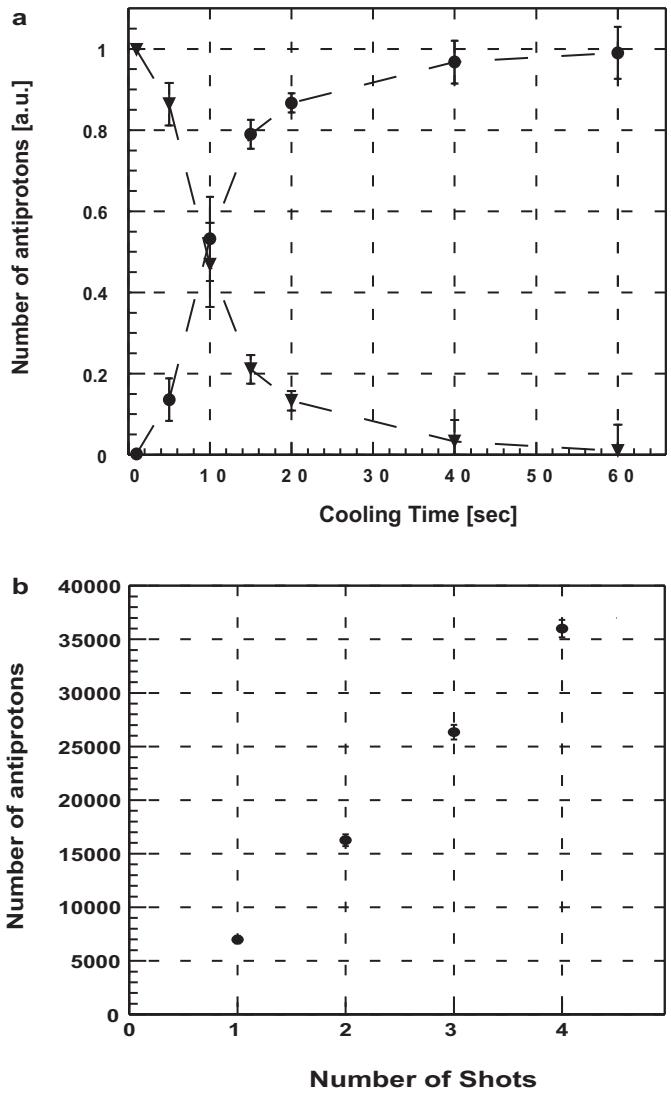

Figure 2.8: The characters of antiproton trap efficiency. **a** Measured fraction of cold (circles) and hot antiprotons (triangles) as a function of their interaction time with electrons. The dashed lines are to guide the eye. **b** Dependence of the number of cold antiprotons on the number of stacked AD shots. Each AD shot contains about 2×10^7 antiprotons. The figures are taken from [11].

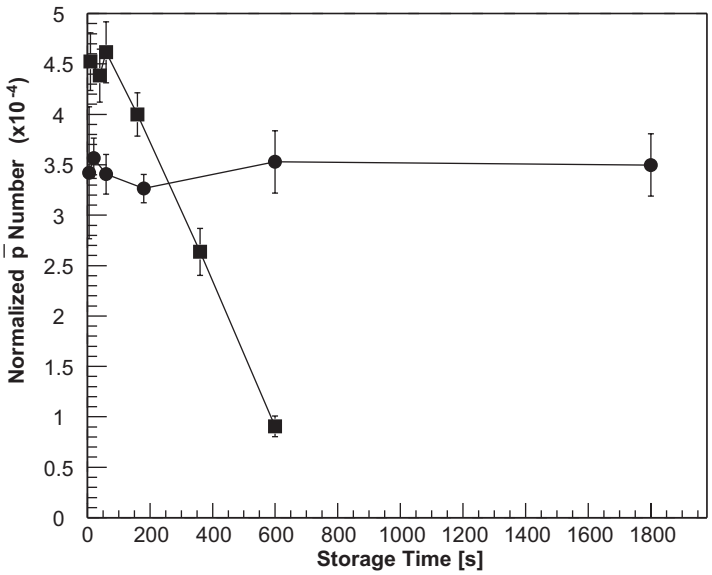

Figure 2.9: Storage time of cold antiprotons with (squares) and without (circles) electrons. The antiproton numbers are normalized to the beam intensity measured with the Hybrid Photo Diode(HPD)-based external beam detectors. The lines are to guide the eye. The figure is taken from [11].

ter the cooling process. The experimental conditions are with a pressure of 10^{-11} mbar (measured in the room temperature region) and with 15 K on the trap. We observed that the electrons reduced the antiproton lifetime; without electrons the half-life of the antiprotons is normally longer than 10 hours.

Antiproton Transfer Cold antiprotons are transferred to the mixing trap by changing the electrode voltage along the traps. Transfer efficiencies greater than 90 % are obtained when electrons and antiprotons are transferred together while a dramatic decrease in the transfer efficiency has been observed if cold antiprotons are moved alone.

In addition, the number of antiprotons stored in the catching trap linearly increase with the number of AD shots (Fig. 2.8**b**).

With the stacking and transferring three AD shots, can prepare about 10^4 cold antiprotons are available at the mixing trap.

The Mixing Trap

The mixing trap in which antiprotons and positrons are merged are composed of 27 cylindrical electrodes with various length (Fig. 2.10). These electrodes can realize a nested trap configuration, where two clouds having opposite signs of electric charges can be confined simultaneously. During the mixing, antihydrogen production can be expected to take place.

The mixing region has three sections, the right well (RW), the left well (LW), and positron well (e^+W) (marked as RW, LW, and e^+W in Fig. 2.10), and each of these sections can make a harmonic potential; LW and RW are used to confine antiprotons and e^+W to confine positrons. The electrodes in the mixing region are made of thinner aluminum (3.25 mm; outside of the mixing region, electrodes are 4 mm thick). The annihilation detectors surround the mixing region. The reason to use aluminum (instead of copper) is to reduce multiple scattering of the annihilation products on their passage to the detector and also to avoid conversion of high energy photons to electrons-positrons pairs, which would be a background if they occurred inside the detection area (see Sec. 3.1.2). One of the electrodes in the positron well is split in four sectors in azimuthal quadrants for the purpose of positron plasma compression using the 'rotating wall' technique (Sec. 4.2.1).

Additional electrodes

There are some additional electrodes toward the positron accumulator to manipulate positrons ($R1-9$ in Fig. 2.10). These electrodes play an important role in the positron transfer from the positron accumulator to the mixing trap (Sec. 2.2.4).

2.2.4 Positron Accumulator

The ATHENA experiment adopted the nitrogen buffer gas system developed at the University of California San Diego group [16, 17, 18], and that system is thought to be one of the most effective positron source. Since this system uses the nitrogen gas for cooling of positrons, ATHENA positron accumulator is located outside of the main magnet where the trap systems (the catching trap and the mixing trap) are mounted with cryogenic and ultra high vacuum environments. Positrons emitted from a radioactive source (^{22}Na) are moderated to $\sim$ eV by a solid-neon [19, 20, 21]. Moderation efficiencies (ab-

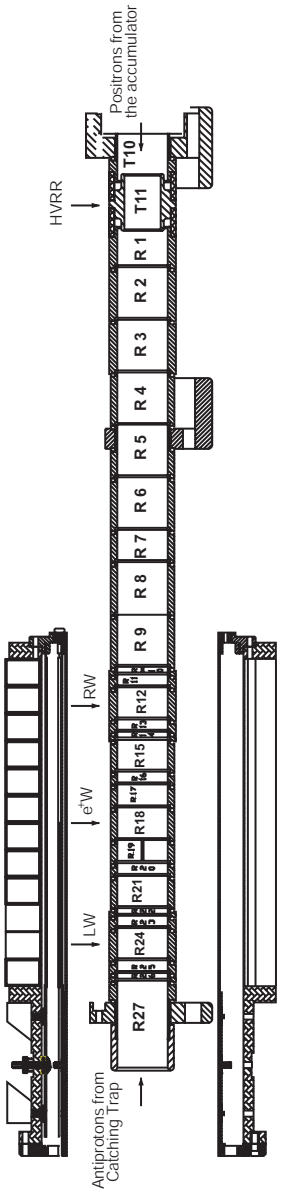

Figure 2.10: The mixing trap. Antiprotons from the catching trap arrive at the left and positrons from the positron accumulator arrive at the right. The 'nested' trap is made of three sections each with the possibility of making a harmonic well. The two outer ones of these (RW and LW) are intended for the antiprotons and the central larger trap (e^+W) is intended for the positrons. The position of the antihydrogen detector is also shown. The figure is taken from [11].

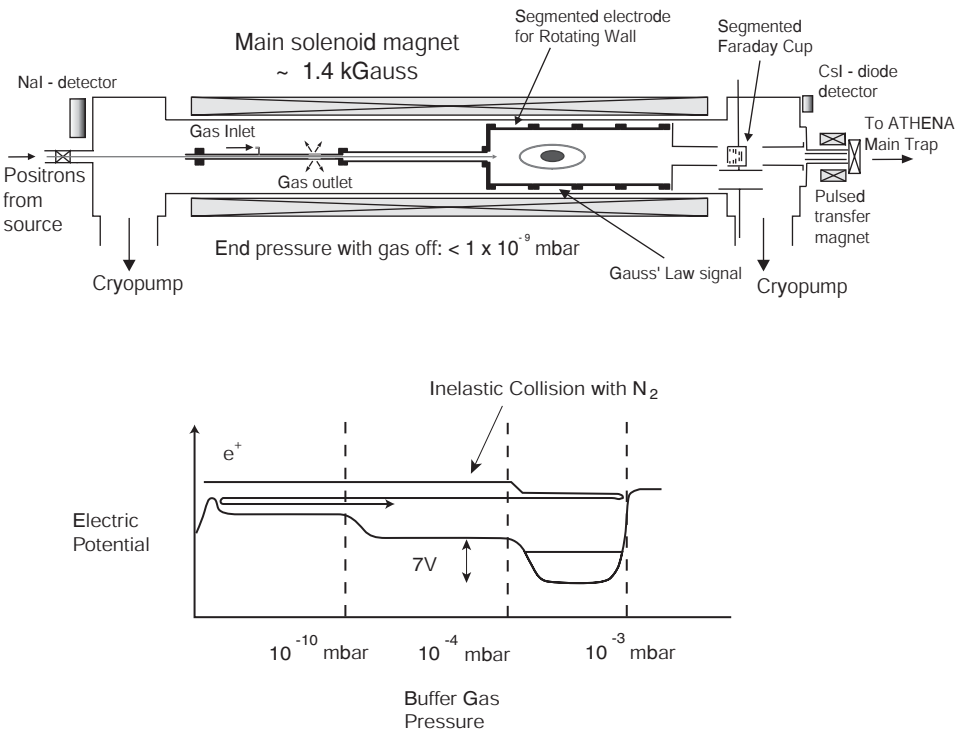

Figure 2.11: Schematic overview of the positron accumulator. The figure is taken from [11].

solute beam intensity divided by the total positron activity of the source) of around 0.4 % are routinely achieved so that beam intensities greater than 5×10^6 positrons per second are available.

Overview of the system and accumulation procedure is schematically drawn in Fig. 2.11. Initial trapping occurs during the first passage of the positron through the trap electrodes by electronic excitation of the nitrogen gas. Such a transition is favored in nitrogen compared to positronium formation, which is the only other major inelastic channel open at our kinetic energies. After trapping, positrons are confined by electric potential in axial direction, and by 0.14 T axial magnetic field in radial direction. Once trapped the positrons continue to lose energy in collisions with the gas, finally reach the deepest part of the well and are accumulated there (see the bottom figure in Fig. 2.11).

One of the trapping electrodes is split into six segments to compress the

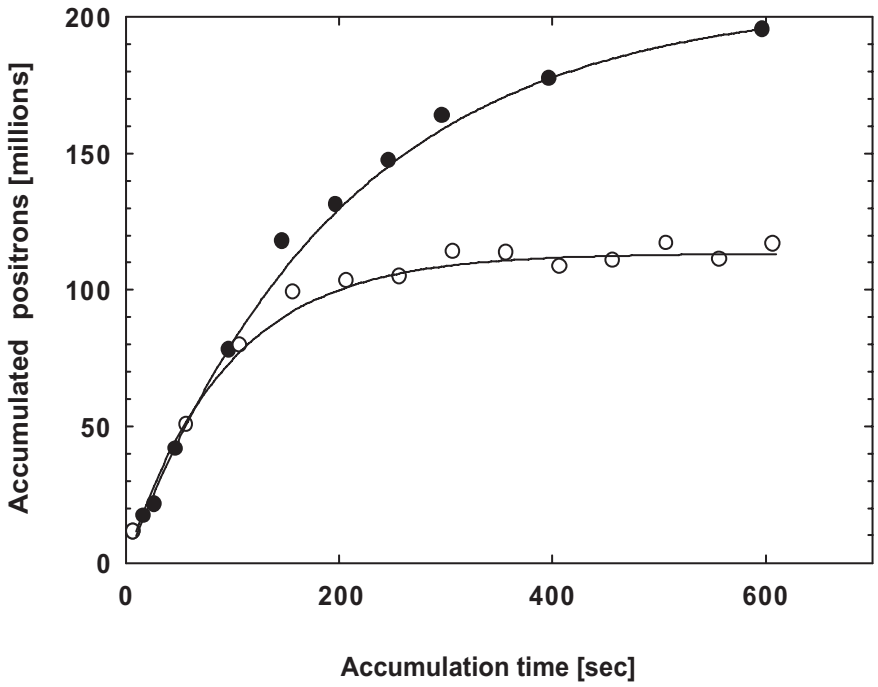

Figure 2.12: The accumulated positron numbers. Accumulation of positrons with (closed circles) and without (open circles) the rotating-wall compression. The figure is taken from [11].

plasma by applying a rotating electric field (the 'rotating wall' technique [22, 31]), and see also Chap. 4. In this technique the rotating electric field exerts torque on the plasma, resulting in its radial compression. This reduces positron losses, leading to a larger number of positrons being accumulated (Fig. 2.12). With the rotating wall, this system can accumulate 1.5×10^8 positrons in 200 s.

Positron Transfer

Positrons are moved from the accumulator with a weak magnetic field (0.14 T) into the main magnet with a strong magnetic field (3 T) through the transfer section located between the two. To avoid the positron radial expansion loss along with magnetic field, the pulse magnet which can make a 1 T field for 1 s is installed in the transfer section (Fig. 2.13). With the pulse magnet, a

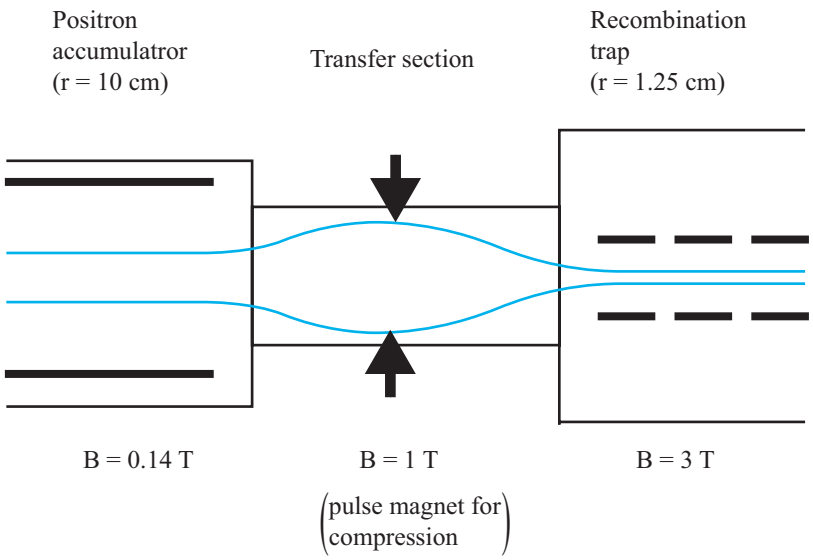

Figure 2.13: Schematic drawing of positron transfer.

transfer efficiency of 50 % is achieved.

2.2.5 Antihydrogen Detector

Once an antihydrogen atom is produced in the mixing trap, the atom can escape from the confinement force because of charge neutrality and should annihilate on one of the trap electrodes creating charged particles (mainly pions) from antiproton annihilation and back-to-back two photons with the energy of 511 keV from positron annihilation. To identify such events, the antihydrogen annihilation detector system composed of silicon micro-strip detectors and CsI crystals is installed surrounding the mixing region (see Fig. 2.17**d**, Fig. 2.14 and Fig. 3.2**a**).

The detector was designed to allow extraction of antihydrogen annihilation signals against background, with specification of a high granularity and a good time resolution. The modules are made as compact as possible in order to be installed into the small limited space between the magnet and the cold nose, and can work at low temperature (140 K) and under the strong magnetic field.

The charged particles from the antiproton annihilation are detected by

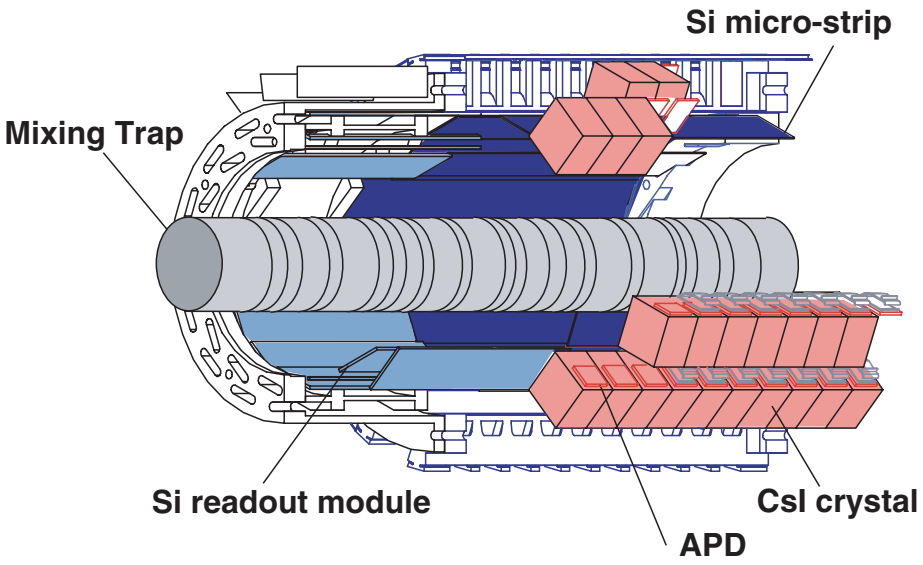

Figure 2.14: Three-dimensional drawing of the antihydrogen detector. The figure is taken from [11].

two layers of silicon strip modules, which allow three-dimensional reconstruction of the antiproton annihilation vertex with a spatial resolution of $\sigma = 4\,\mathrm{mm}$ by straight line extrapolation of the charged particle tracks. Photons from positron annihilation are detected by the CsI crystals, which have the photo-peak efficiency of 25 % at 511 keV. The segmentation of 192 crystals (16 modules containing 12 rows each surround the cold nose) allows identification of two back-to-back 511 keV photons.

Design of the Detector

Fig. 2.14 shows a three-dimensional drawing of the annihilation detector, which has cylindrical dimensions of 75 mm inner and 140 mm outer diameters. The length is 250 mm. The inner and outer diameter are constrained by the size of the cold nose vessel and the superconducting bore magnet. The inner two layers contain 16 double sided silicon micro-strip modules with 162 mm length in active area. The outer layer contains 16 module with CsI crystals arranged around the beam axis. Each module has a row of 12 crystals ($17 \times 17.5 \times 13\,\mathrm{mm}^3$) bonded to the aluminum support of 500 μm thickness.

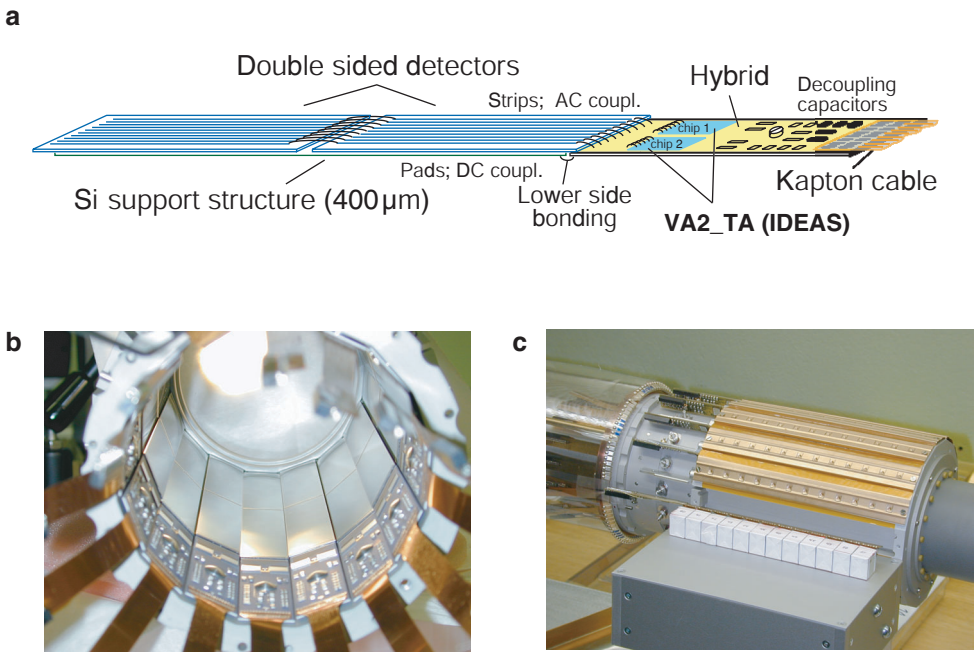

Figure 2.15: The detector modules. **a,** A schematic drawing of the electronics. **b,** A photograph of silicon micro strip module. **c,** The photograph of CsI crystals.

The micro-strip silicon modules consist of two double sided (p and n) sensors (SINTEF, Norway, $81.6 \times 19\,\mathrm{mm}^2$ with a thickness of $380\,\mu$m) and a multilayer ceramic hybrid, 2 mm thick (Fig. 2.15**a** and Fig. 2.15**b**). The sensor p-sides are segmented into 384 AC coupled strips with a pitch of 46.5μm (a gap between each strips is 14.5μm). Every third strip is read out while the two intermediate strips are floating. The readout strips are bonded to the pitch adapter integrated and connected to the 128 channels readout chip (VA2_TA) in hybrid. In sensor n-sides contain 128 DC coupled pads ($1.25 \times 18\,\mathrm{mm}^2$) are bonded oriented perpendicular to the strip line at the p-side. 128 signals from pads can be delivered to the second VA2_TA readout chip through the thin gold plated aluminum lines.

Pure CsI crystals (CRISMATEC, France;Fig. 2.15**c**) used for detection of 511 keV photons achieve a good light yield at low temperature (about 50,000 photons/MeV at 80 K [24]). The crystals are read out by avalanche photo diodes (APD), type S8248 (Hamamatu, Japan) with the dimensions

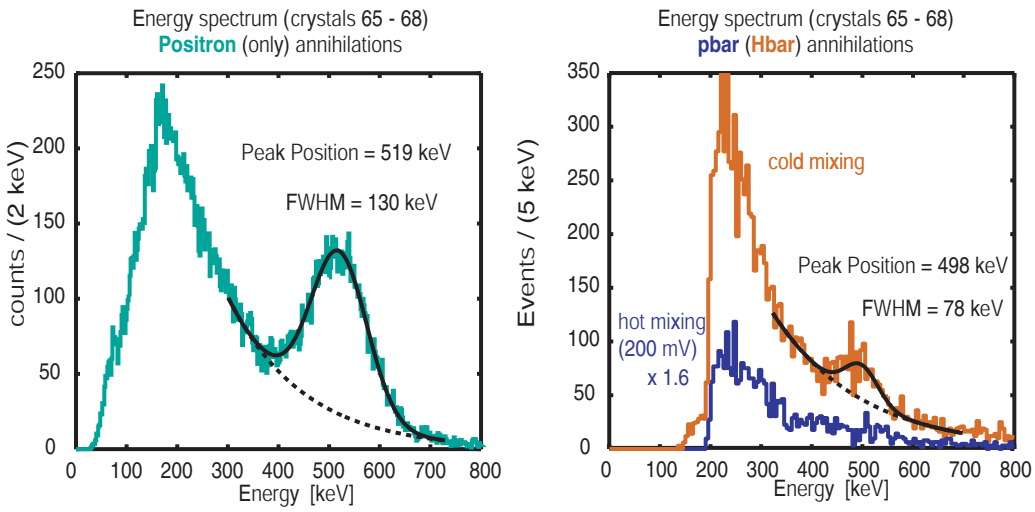

Figure 2.16: A typical energy spectrum of gamma rays measured with the CsI crystals. The data were taken during a dedicated positron run (left) and during a normal runs (right). The figures are taken from [11].

of $5 \times 5\,\mathrm{mm}^2$. A typical energy spectrum using a radioactive source ^{22}Na at 150 K is shown in Fig. 2.16. Clear peak signal was obtained at 511 keV with a good signal-to-noise ratio and energy resolution was $\simeq 18\,\%$ at FWHM.

The 16 ceramic hybrids for silicon micro-strip are each connected parallel to cylindrically bent patch panel through Kapton cables. These patch panels at 140 K region are connected to five D-sub 50 pin feedthroughs at the vacuum flange of CF150 by 1.5 m shielded cables (LakeShore, USA; 1 mm diameter $50\,\Omega$ cryo-cable with drain wire and aluminum shielding).

Installation of the Instruments

For easy understanding the features in design of the ATHENA apparatus, the system configuration is explained with some photo pictures following the installation of the instruments (Fig. 2.17; the alphabets marked at each items correspond to the those at photos).

a). The trap systems are settled with their cable lines. All the lines are through the special tubes made of stainless steel to keep the tolerance.

b). The whole trap systems are installed into the cold nose chamber that is made of the aluminum. The cold nose physically separates the ultra high vacuum region from the place where the antihydrogen detector is mounted.

c). The cold nose is wrapped by the thermal insulator, and separates the both systems thermally.

d). The detectors are mounted covering the almost whole the mixing region. The whole systems are housed in the bore of superconducting solenoid magnet.

2.2.6 Control and Acquisition system

In ATHENA experiment, the annihilation events are recorded by the fast data acquisition system, while the trap electrodes are controlled by the slow control system. While the former is by random triggers, the latter is synchronized to the AD machine cycle. The details of each part are as well as of analysis software are described below.

Data Acquisition system

The data acquisition system (DAQ, Fig. 2.18) produces a record of all activities in the apparatus: detector read out, state of the apparatus, voltage and timing information from the control system. All the data are read out via VME and GPIB modules readout by a LabVIEW program, and written to a database. The dead time-free acquisition is achieved by the multi-hit time stamp units (Struck SIS 3806) with 1 ms accuracy. This module has switching memory system; two FIFOs are inside of the module, and the active memory is switched by the trigger.

Slow Control system

The control system is required to control all electrodes of the trap system, and to manage communication with the computers (Fig. 2.19). Voltages on the electrodes of the mixing trap are supplied by triggerable DAC's (Joerger VDACM and National Instruments DAC (6713)). The interface to the control system is written in LabVIEW; the DACs are able to provide voltage

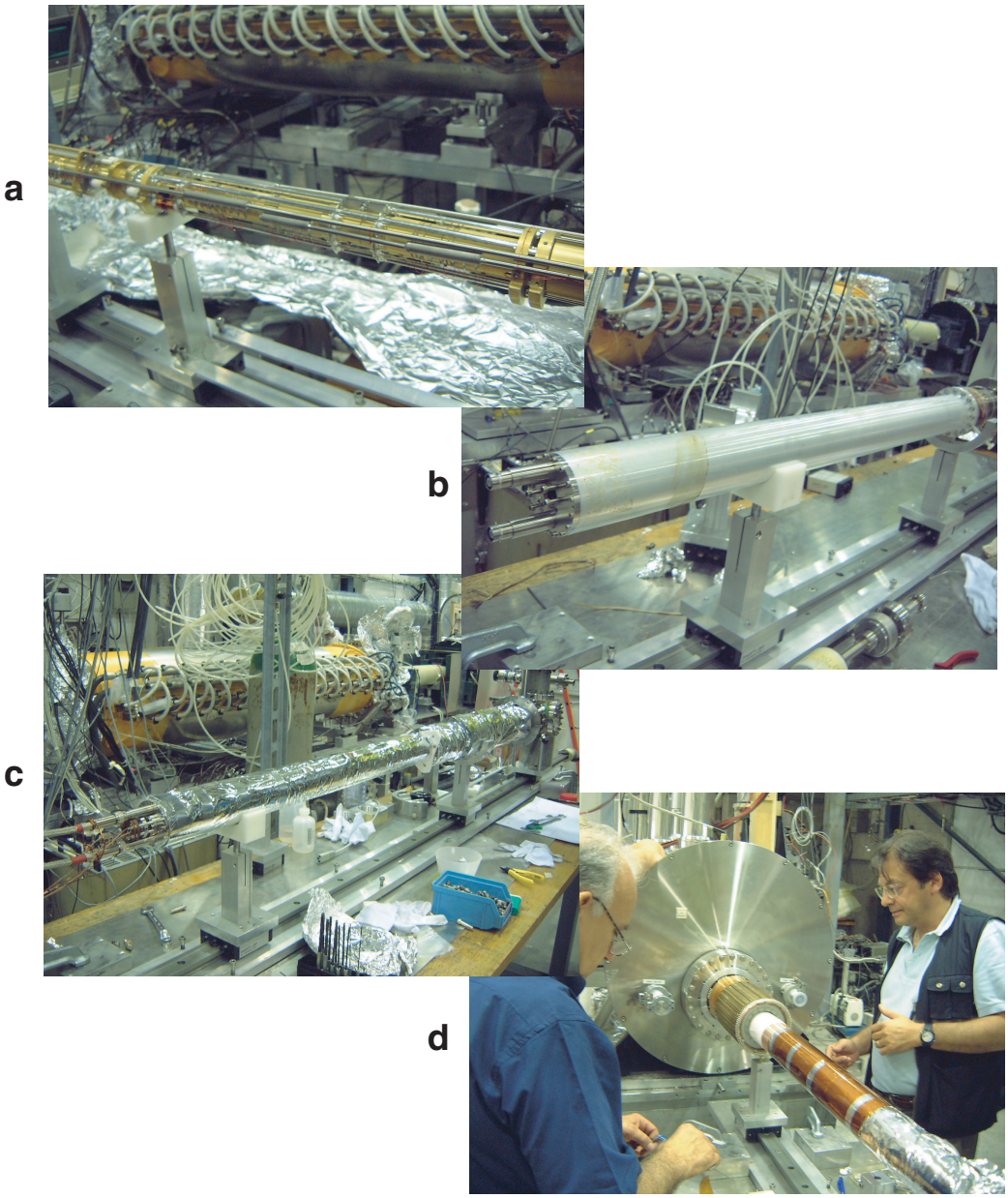

Figure 2.17: The pictures showing the installation procedure.. **a).** The trap system and its cable lines. **b).** The cold nose housing the trap systems. **c).** The cold nose wrapped by the thermal insulator. **d).** The detector is mounted and all the instruments are put in the bore of superconducting solenoid magnet.

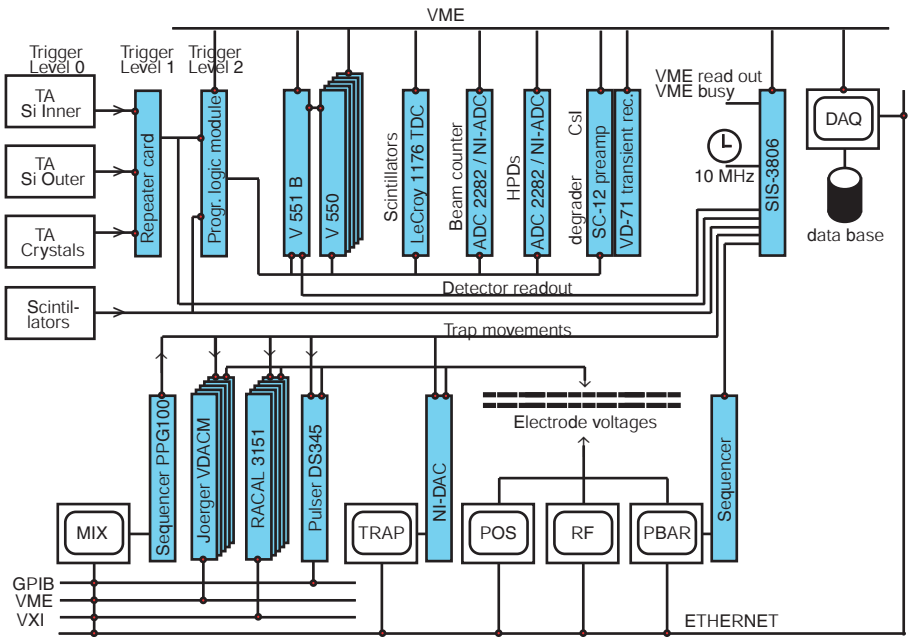

Figure 2.18: Diagram of the data acquisition system. The figure is taken from [11].

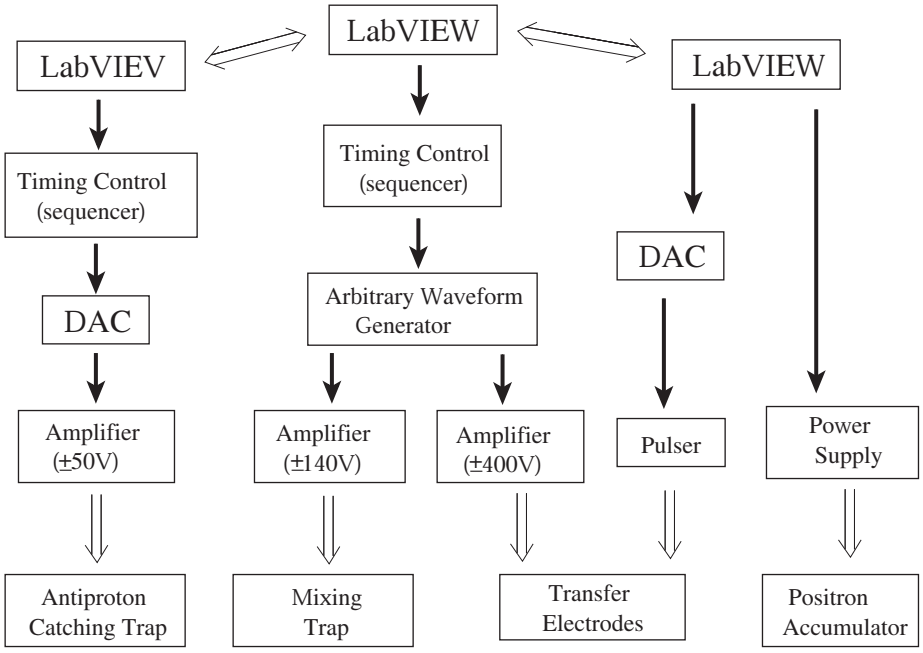

Figure 2.19: Diagram of the slow control system.

sequences of several thousand steps and lasting several hours with microsecond precision.

Analysis Software

Online system The ATHENA online system was written in C++ by using the ROOT package [25]. The data are saved in a raw file by using a private binary format without any compression to obtain the maximum possible speed during acquisition.

Offline system The ATHENA offline software is written in C++ and uses a set of ROOT macros. It decodes the detector response, reconstructs the interaction points of the particles in the inner and external silicon layers, associates the tracks to these points (pattern recognition), finds the vertex of the charged particles and selects the crystals with 511 keV-signals. Some batch macros give a set of histograms to control both vertex positions of the annihilations and detector performances.

A Monte Carlo (MC) code has been written to study the optimum selection criteria for antihydrogen events and to evaluate the probability that a selected antihydrogen event may be a background event. The MC program was conceived as a C++ interface between ROOT and the GEANT code for the generation of simulated data from nuclear physics experiments [26].

2.2.7 Plasma techniques

In ATHENA experiment the large amount of charged particles are accumulated within the small volume inside of the Penning trap by the electromagnetic field. Trapped particle can be treated as a plasma, if Debye length λ_D defined by $(\epsilon_0 k_B T/n_0 e^2)^{1/2}$ (ϵ_0 is the permittivity of the vacuum, k_B is the Boltzmann constant, n_0 is the density of cloud and e is electric charge) is less than the size of cloud. In our case, electrons and positrons with the density of over $10^8\,\mathrm{cm}^{-3}$ can be treated as plasma if the particle could be cooled down to the trap temperature (15 K) by synchrotron radiation. Plasma manipulation techniques which can achieve useful operations for producing antihydrogen, are developed and are installed.

'Plasma mode' system

In the trap, plasma has collective oscillations, and their frequencies are called 'plasma mode frequencies'. The axial motion of the cloud is called 'dipole mode' and the internal motion with two segmented part is 'quadrupole mode', as shown in Fig. 2.20. The frequencies depend on plasma shape, temperature and number of particles, thus these frequencies can be useful probes for plasma diagnosis. A nondestructive plasma monitoring system using the plasma mode frequencies, called 'plasma mode system' is developed in the ATHENA experiment.

The setup is schematically shown in Fig. 2.21. Two of the electrodes in the positron trap region (e^+W) are connected to a vector network analyzer. One electrode is for inducing the positron plasma oscillation, and the other is for detecting the response of the plasma. The observed lowest two order of plasma mode signals are shown in Fig. 2.22. From these frequencies, the plasma shape (radius, length), number, density and temperature can be obtained. Length and number come from the line shape of the dipole mode frequency, density and aspect ratio (length/radius) are from the combination

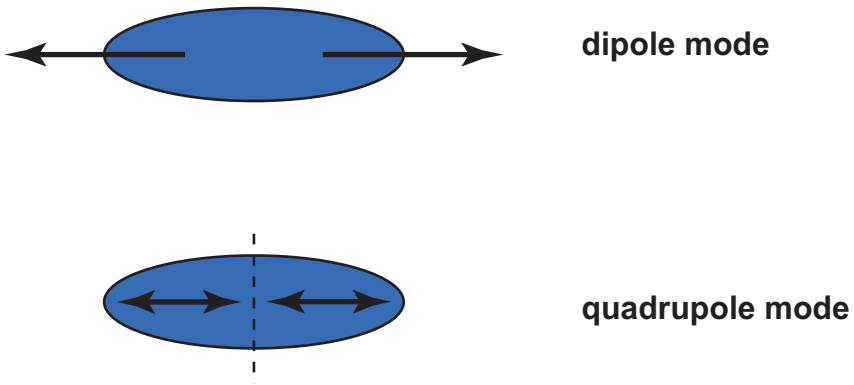

Figure 2.20: The image of plasma mode oscillation.

of the dipole mode frequency and the quadrupole mode frequency, and will be discussed in detail in Sec. 4.2.2 (also [15]).

RF heating

Recently a theory has been developed in the cold fluid limit where correlations between particles are neglected [35, 36], thus plasma can be treated with a fluid theory. Though we can calculate plasma mode frequency from this cold fluid theory, an observed frequency should be different from the predicted one because this theory dose not include the correlations between each particles. From the deference between the experimental and calculated frequencies, we can estimate plasma temperature.

Analytical treatment which consider the temperature effects on the quadrupole mode frequency is proposed [18]. This model predicts a shift in the quadrupole mode frequency from the calculate frequency ω_2^c to observed frequency ω_2;

$$(\omega_2)^2 = (\omega_2^c)^2 + 20[3 - g(\alpha)]\frac{k_B T}{mL^2}, \tag{2.2}$$

$$g(\alpha) = \frac{\alpha^2}{2}\frac{\omega_p^2}{(\omega_2^c)^2}\frac{\partial^2 A_3}{\partial \alpha^2}, \tag{2.3}$$

where α is aspect ratio defined as length/diameter of plasma, $A_3 = 2Q_1(k_2)/(\alpha^2 - 1)$, Q_1 is Legendre function of the second kind, and $k_2 = \alpha(\alpha^2 - 1)^{-1/2}$. By applying this theory to the quadrupole mode, we try to estimate plasma temperature from the mode frequency shift.

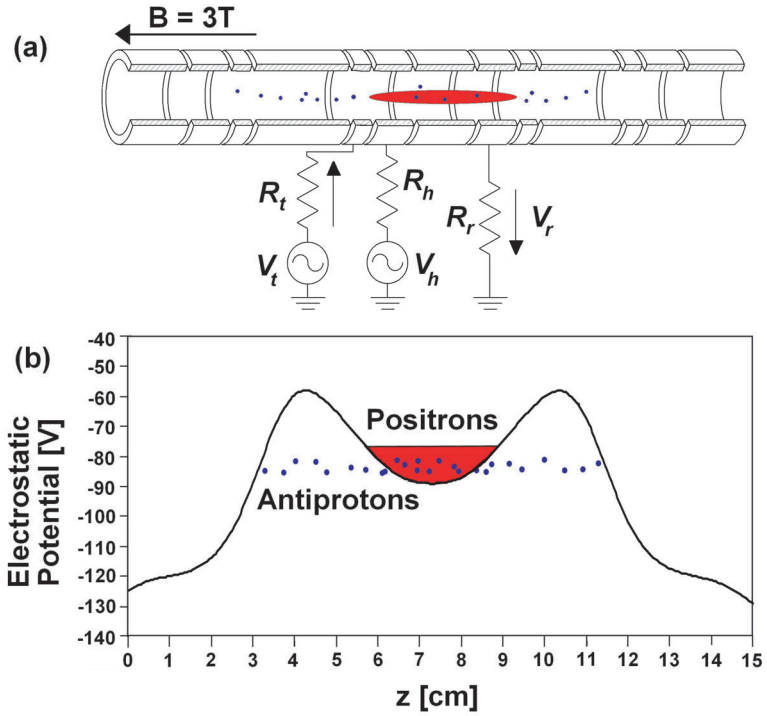

Figure 2.21: The schematic view of the plasma mode system. **(a)** Trap electrodes with the heating and mode detection electronics. The shape of the positron plasma is drawn schematically. **(b)** The axial potential of the ATHENA nested trap is shown and the motion of the positrons and the antiprotons indicated schematically. The figures are taken from [15]

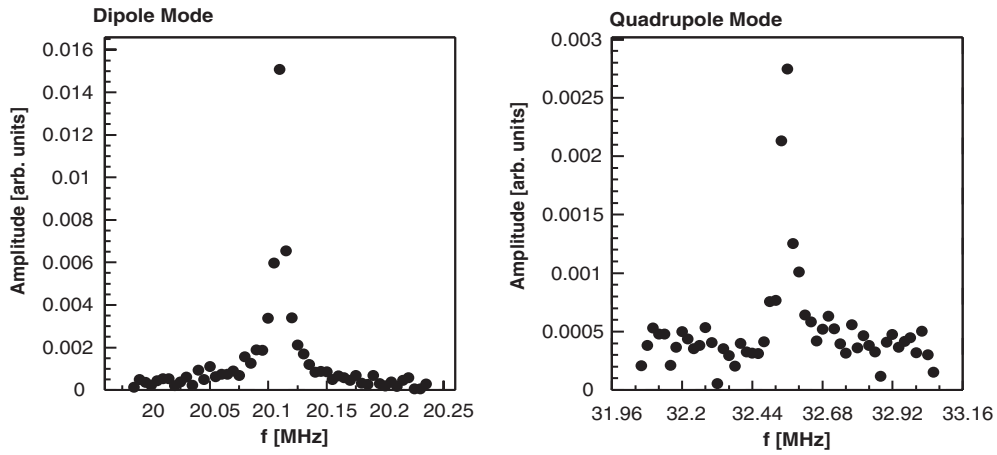

Figure 2.22: Measurement of the amplitude of the first two low-order axial modes as a function of the drive frequency. The figures are taken from [11]

In the ATHENA, the temperature of positron cloud can be changed and controlled by using RF heating which is adjusted to the axial frequency (the dipole mode frequency). The drive frequency from the vector network analyzer is set to cover the range around the dipole mode frequency and the temperature can be estimated from the the shift of the quadrupole mode frequency. With this scheme the positron temperature can be controlled (Fig. 2.23).

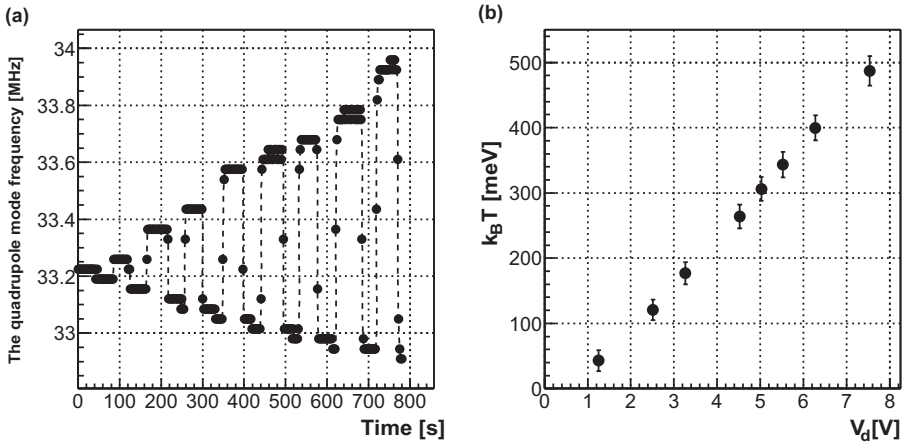

Figure 2.23: The typical behavior of plasma mode frequencies at RF heating. **(a)** Time evolution of the quadrupole mode frequency during a heating off-on cycle. The different frequency shifts correspond to different heating amplitudes. The drift of the frequency in the unperturbed intervals is due to the plasma expansion, and it is consistent with the normal evolution of the unperturbed plasma. **(b)** Dependence of the temperature on radio-frequency signal amplitude for the same cycle. The figures are taken from [15]

Chapter 3

Cold Antihydrogen

The details of the first production and detection of cold antihydrogen are described in this chapter.

3.1 Experimental Procedures

3.1.1 Production scheme

For producing antihydrogen, we prepare large amounts of antiprotons and positrons:

Antiprotons Antiprotons from the AD are captured and cooled in the catching trap. Three AD shots are stacked in the catching trap. After transferring to the mixing trap, 10^4 cold antiprotons are available for mixing.

Positrons Positrons provided by a radioactive source are accumulated in the accumulator. In 200 s, 1.5×10^8 positrons can be accumulated. The positrons are then transferred to the main magnet, with an efficiency of some 50 %, so that 7×10^7 positrons are available for mixing.

In order to merge the two kinds of charged particles with opposite signs of charges in the same region, a special potential shape (called 'nested trap') is used. The nested trap is composed of three potential parts (Fig. 3.1). One central well is used for the positron confinement ('e^+W') and the both edge parts are used for antiprotons ('RW' and 'LW').

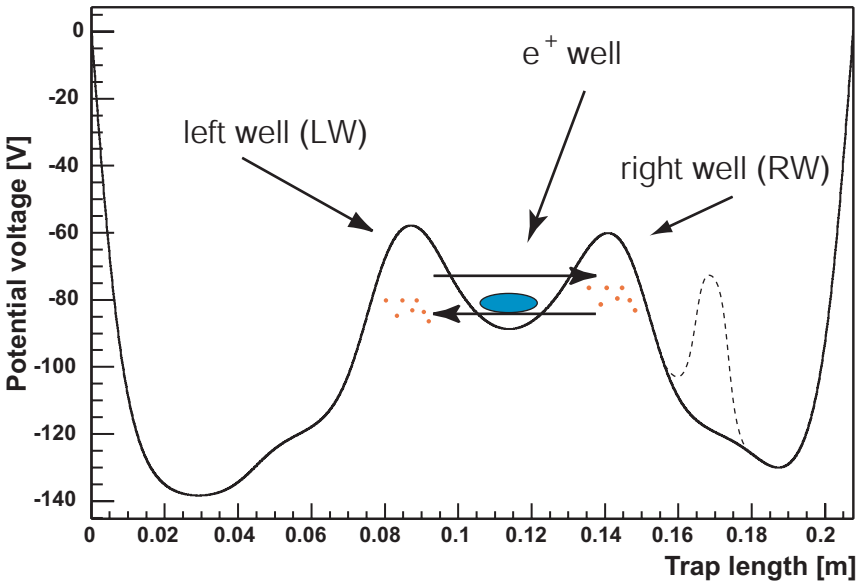

Figure 3.1: The configuration of the nested trap. The potential voltage in graph gives the real value used for antihydrogen production on the central axis of the trap system. The antiprotons go back and forth, and can interact with the positrons many times. The dashed line is the potential immediately before antiproton injection

The mixing sequence proceeds as follows, first positrons are moved to the positron central well from the accumulator. Meanwhile the antiprotons and electrons are moved together from the catching trap to their injection place, located next to the right well (see Fig. 3.1). Electrons are kicked out by short electric pulse before injection. After waiting for more than 10 sec after positron transfer, the antiprotons are injected into the positrons. The mixing continues for 190 s.

3.1.2 Antihydrogen Detection scheme

If antihydrogen atoms are produced during mixing cycle, they escape from the confinement of electric field, annihilate on the trap electrodes and produce charged particles (mainly pions) from antiproton annihilation and two 511 keV photons from positron annihilation. We utilized the silicon detectors and CsI crystals to identify antihydrogen events in the following way:

Vertex reconstruction of antiprotons Antiprotons normally annihilate into a few charged or neutral pions. These pions are detected by the two layers of silicon micro-strip detectors. The path of a charged particle passing through both silicon micro-strip layers (green lines in Fig. 3.2**a**) can be reconstructed, and two or more intersecting tracks allow to decide the position or vertex of antiproton annihilation. The uncertainty in vertex determination is approximately 4 mm ($1\,\sigma$) and is dominated by the unmeasured curvature of the charged pions' trajectories in the magnetic field.

Opening angle Positron annihilation with an electron yields two or three photons. Our positron detector consists of 16 rows, each row containing 12 CsI crystals which are designed to detect two photons with the energy of 511 keV. These two 511 keV photons should be emitted back-to-back if they come from antihydrogen annihilation. The two CsI crystals detecting 511 keV photon signals within the same window ($5\,\mu$s) at which antiproton annihilation vertex reconstruction is succeefully achieved, are selected. And the opening angle, $\theta_{\gamma\gamma}$, insisted by two 511 keV photons can be got by extrapolating photon paths from these two CsI's to the antiproton annihilation vertex (red wave lines in Fig. 3.2**b**). For an antihydrogen event, this angle should be 180° (or $cos(\theta_{\gamma\gamma}) = -1$).

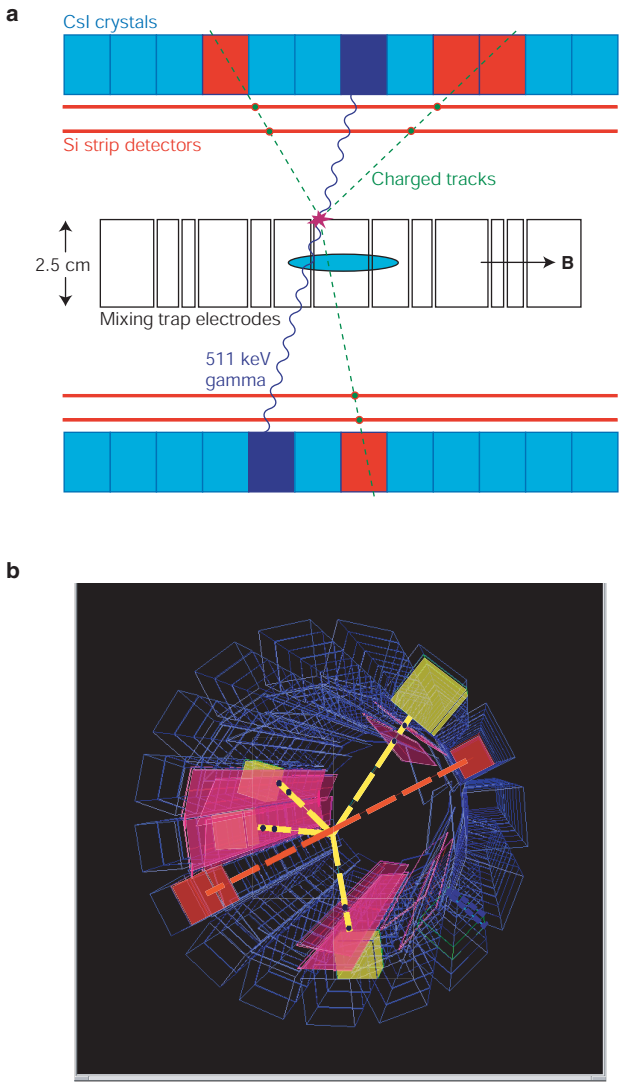

Figure 3.2: Detection scheme for antihydrogen annihilation event. **a,** Schematic diagram, in axial section, of the ATHENA mixing trap and antihydrogen detector. The cylindrical electrodes and the position of the positron cloud (blue ellipse) are shown. A typical antihydrogen annihilation into three charged pions and two back-to-back 511-keV photons is also shown. The arrow indicates the direction of the magnetic field. The detector active volume is 16 cm long and has inner and outer diameters of 7.5 cm and 14 cm, respectively. The figure is taken from [48]. **b,** The typical antihydrogen annihilation event reconstructed by the ATHENA analysis software.

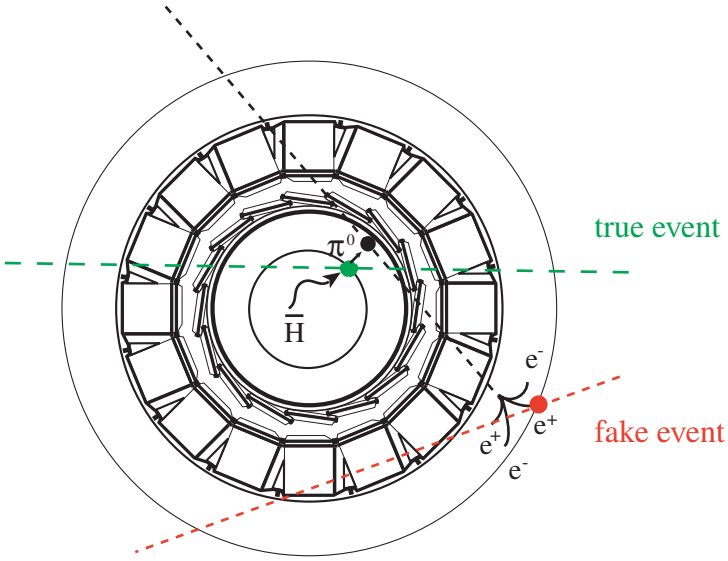

Figure 3.3: The origin of 511 keV γ-ray background. γ-ray, which is generated from neutral pions from nucleus-antiproton annihilation, yields the electron-positron shower. These positrons make 511 keV γ-rays, which are detected by the crystals as background.

Background Estimation Main background comes from π^0 decays, which can produce positrons near the detection volume (Fig. 3.3). The annihilation of these positrons, detected in coincidence with charged pions, can mimic antihydrogen events.

$$\begin{aligned} \mathrm{p} + \bar{\mathrm{p}} &\rightarrow \pi^0,\ \pi^{\pm} \\ \pi^0 &\rightarrow 2\,\gamma \rightarrow \mathrm{e}^+ + \mathrm{e}^- \end{aligned}$$

However the antihydrogen events can be identified from these backgrounds due to the lack of back-to-back angular correlation in the background signals. Monte Carlo simulation with ATHENA setup is shown in Fig. 3.4. A clear peak can be seen at the angle of 180° (or $cos(\theta_{\gamma\gamma}) = -1$), only for the antihydrogen events, as expected above.

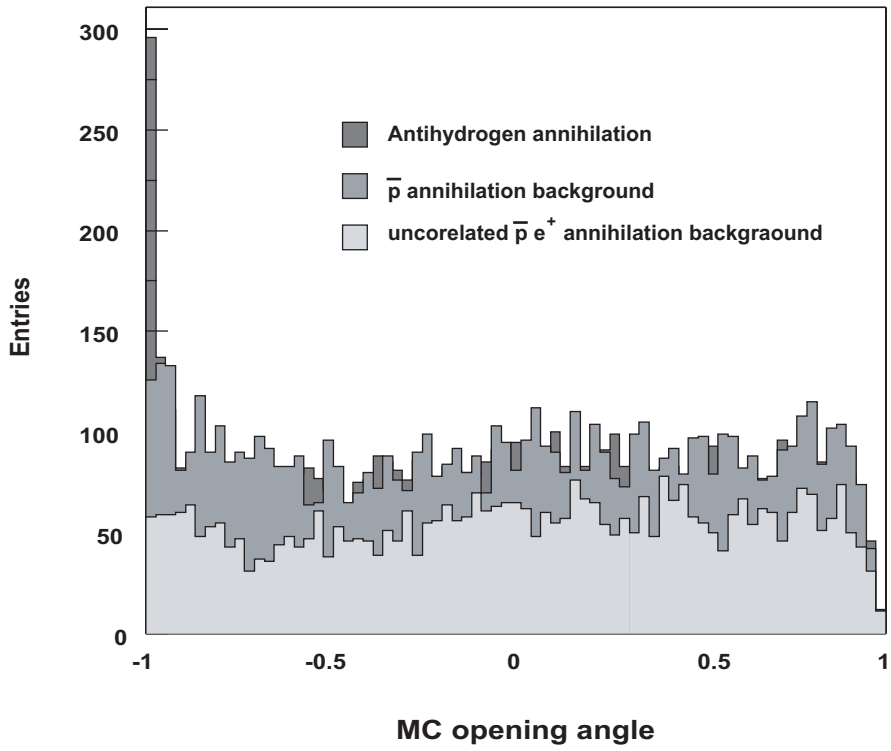

Figure 3.4: The expected opening angle distributions using a Monte Carlo simulation. From the dense to weak gray color, each histograms corresponds to; $cos(\theta_{\gamma\gamma})$ distribution of the opening angle for antihydrogen annihilation (most dense), the antiproton annihilation background (middle) the uncorrelated antiproton (or positron-electron) annihilation background (weakest).

3.2 Experimental Data

3.2.1 Comparison of different mixing schemes

To produce antihydrogen atoms, we fill a positron well with about 7.5×10^7 positrons and then approximately 10^4 antiprotons are injected to the mixing region. The mixing time is 190 sec, after which all particles are dumped and process was repeated. We refer to this procedure as 'cold mixing'.

A second type of procedure, 'hot mixing', involves radio frequency heating of the axial motion of positron plasma applied the plasma manipulation technique (Sec. 2.2.7). During the mixing cycle with antiprotons, the positrons are maintained at a temperature of several thousand kelvin. The positron temperature is monitored using the plasma mode analysis technique (see Sec. 2.2.7 and Sec. 4.2.2). Both radiative process and three-body process should be effectively suppressed at this temperature even though the antiprotons and positrons still interact.

For comparison and for investigation of background processes, we loaded antiprotons into the interaction region without positrons and accumulated data. This data is referred to as 'antiproton only'.

For 'cold mixing', interaction of the two species is immediately apparent by the mode analysis, and the antiprotons are rapidly cooled (less than 1 sec) to the energy corresponding to that of the positron well. The cooling process was observed by lowering the wall of the antiproton right and left well to various levels and recording the antiprotons loss on the external scintillators. During the mixing cycle, no positron loss was observed. At the start of cold mixing, a rapid jump in the rate of antiproton annihilation was observed. No such effect was seen in the hot mixing cycle. At early times, the number of trigger at the cold mixing on the silicon strip detector was about 10 times higher than that at the hot mixing. The positron loss during hot mixing is indistinguishable from that during cold mixing.

To search antihydrogen in the sample of events having a vertex and two photons, the opening angle $\theta_{\gamma\gamma}$ between the lines connecting the vertex point to the geometric centers of the two hit crystals was calculated for each event. For an antihydrogen event, this angle should be 180° (or $cos(\theta_{\gamma\gamma}) = -1$).

The opening-angle distribution for cold mixing is compared for hot mixing in Fig. 3.5**a**. The cold mixing data display a clear enhancement of events close to $cos(\theta_{\gamma\gamma}) = -1$, indicative of antihydrogen production. No such

enhancement is visible in the hot mixing data. In Fig. 3.5**b**, antiproton only data are shown. There is no peak at $cos(\theta_{\gamma\gamma}) = -1$. Also shown in Fig. 3.5**b** is the result of analysis of the cold mixing data using an energy window excluding the 511 keV peak. There is no peak at $cos(\theta_{\gamma\gamma}) = -1$ either.

3.2.2 Discussion

The shape of the $cos(\theta_{\gamma\gamma})$ distribution predicted by Monte Carlo analysis of our detector for antihydrogen annihilation (see Fig. 3.4) agrees with that of the cold mixing measurement. The dominant background for the experiment must be cause by a neutral pions produced in antiproton annihilations. The antiproton-only data (Fig. 3.5**b**) rule out this process as the source of antihydrogen-like signal seen in the cold mixing cycle.

Other sources of background, such as cosmic rays and background from accelerator operation (AD beam injection and extraction) can also be excluded, since the probability for accidental coincidence of the antiproton and positron annihilation is negligible during mixing as determined from measured trigger rates for each part of the detector. Furthermore, Monte Carlo simulations of this background indicate no enhancement in opening angle at 180°.

3.2.3 Further Confirmation

Further confirmation of antihydrogen production can be seen in difference between the cold and the hot mixing. The distribution of all antiproton annihilation projected onto a plane perpendicular to the magnetic field is shown in Fig. 3.6**a**. In the cold mixing, a clear image of the trap electrodes is obtained, consistent with neutral anti-atom annihilation on the wall. This observation also implies that many more antihydrogen atoms are produced than are actually identified through the opening angle correlation.

On the other hand, the vertex distribution for the hot mixing shows no evidence of annihilation on the trap wall (Fig. 3.6**b**). The antiproton annihilation in the central region of the trap probably come from collisions with the residual gas or with trapped ions in the positron plasma. The average annihilation rate for hot mixing is about a factor of 4 smaller than that for cold mixing.

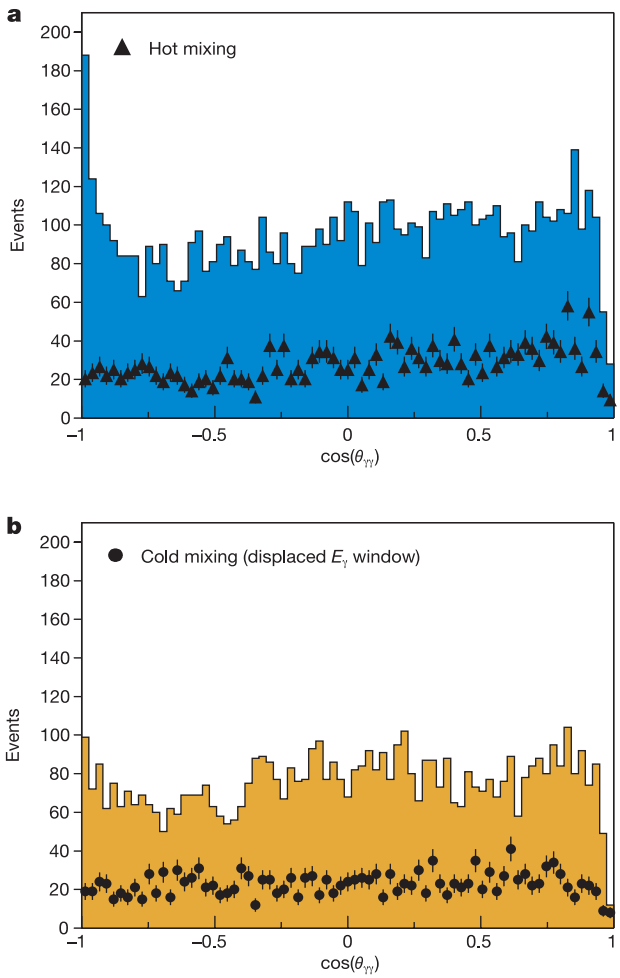

Figure 3.5: Experimental data. **a,** The number of events passing the selection criteria is plotted against the cosine of the opening angle $\theta_{\gamma\gamma}$ (see text for definition). The histogram is for cold mixing data (blue background). A total of $7,125$ events, out of a sample of $103,270$ reconstructed vertices, have two clean (but not necessarily back-to-back), detected photons in the 511 keV energy window. The data represent 165 mixing cycles. Filled triangles represent hot mixing data and are scaled by 1.6 to depict the same number of mixing cycles. **b,** The opening angle distribution (orange histogram) for antiproton-only data ($99,610$ vertices reconstructed, $56,584$ clean events plotted). The filled circles represent cold mixing data, analyzed using an energy (E_γ) window displaced upward so as not to include the 511 keV photo peak; no angular correlation of photons is seen. The figures are taken from [48].

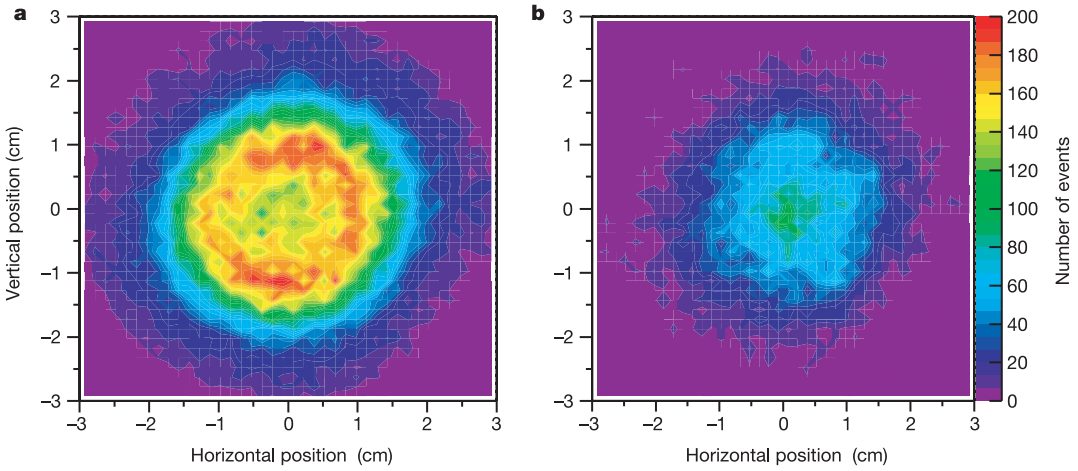

Figure 3.6: Color contour plots of the distribution (obtained by projecting into the plane perpendicular to the magnetic field) of the vertex positions of reconstructed events. **a,** Cold mixing. All reconstructed antiproton annihilation vertices from the mixing region are plotted. The trap inner radius is 1.25 cm. The annihilations are centered on a slightly smaller radius, in agreement with our Monte Carlo simulations. (Some events appear to be outside of the trap radius owing to vertex reconstruction errors.) **b,** The same plot as above, but for hot mixing. These data are normalized to represent the same number of mixing cycles (165) as those in **a**. The figures are taken from [48].

3.2.4 Conclusion

If the data only in the range $cos(\theta_{\gamma\gamma}) < -0.95$ is taken into consideration, 131 ± 22 events with a reconstructed vertex and a pair of back-to-back 511 keV photons, are detected above a conservatively scaled antiproton-only background. With an upper limit of the detection and reconstruction efficiency of 2.5×10^{-3}, we estimate that at least $50,000$ antihydrogen atoms were created during the cold mixing.

Chapter 4

Further Study with the plasma control techniques

We succeeded in producing a large amount of cold antihydrogen atoms. This is a milestone for the study of antimatter and the first necessary step towards laser spectroscopy aiming at the high-precision test of CPT. However, there are still many points which need to be clarified. For example, laser spectroscopy requires antihydrogen in the ground ($1s$) state, but we do not yet know what fraction of antihydrogen we observe is in the ground state.

The processes contributing to production of cold antihydrogen are thought to be the radiative process and the three-body process. Of the two, the radiative process predominantly populates the ground state. Hence it is important to understand what fraction of the produced antihydrogen is due to the radiative process. Since the two processes depend differently on the positron density n_{e^+} (and also on temperature T), we made use of the plasma control techniques to modify the positron density, and studied how the antihydrogen production rate depends on this parameter.

First, we discuss the theoretical model of the radiative process and the three-body process, in order to clarify the motivation of this measurement. Second the plasma techniques used for the positron parameters are explained. Third, the details of the method we developed are described, and then the effect on antihydrogen production rate (mixing with the different kinds of positrons) is discussed.

4.1 Motivation

In ATHENA experiment, the main antihydrogen production processes are thought to be the radiative process and the three-body process. As shown in Table 4.1, the two processes have different temperature and density dependences. It is also important to note that the final quantum states differ significantly [27, 29].

When an antihydrogen atom is produced by capturing a positron, the excess energy should by carried out by something. In the case of the radiative process, a positron is captured by an antiproton and the excess energy is carried by a photon,

$$\bar{\mathrm{p}} + \mathrm{e}^+ \quad \rightarrow \quad \bar{\mathrm{H}} + \gamma.$$

In the case of three-body process, one antiproton and two positrons are concerned. One of the positrons are captured by an antiproton and the other positron carries the excess energy,

$$\bar{\mathrm{p}} + \mathrm{e}^+ + \mathrm{e}^+ \quad \rightarrow \quad \bar{\mathrm{H}} + \mathrm{e}^+.$$

Theoretically, the production rates of these processes scale with positron temperature T_{e^+} and density n_{e^+} as [27, 28, 29];

$$\mathrm{radiative}: \quad R \propto n_{\mathrm{e}^+} T_{\mathrm{e}^+}^{-1/2}, \tag{4.1}$$

$$\mathrm{three-body}: \quad R \propto n_{\mathrm{e}^+}^2 T_{\mathrm{e}^+}^{-9/2}. \tag{4.2}$$

These formula indicate that we should be able to disentangle the two processes by studying the temperature and density dependence of production rate.

	Radiative process	Three-body process
Temperature dependence	$T_{\mathrm{e}^+}^{-1/2}$	$T_{\mathrm{e}^+}^{-9/2}$
Density dependence	n_{e^+}	$n_{\mathrm{e}^+}^2$
Final quantum state	$n < 10$	$n \gg 10$
Stability (re-ionization)	high	low

Table 4.1: Typical parameters of produced antihydrogen. The energy level of the captured positron is determined by the production process.

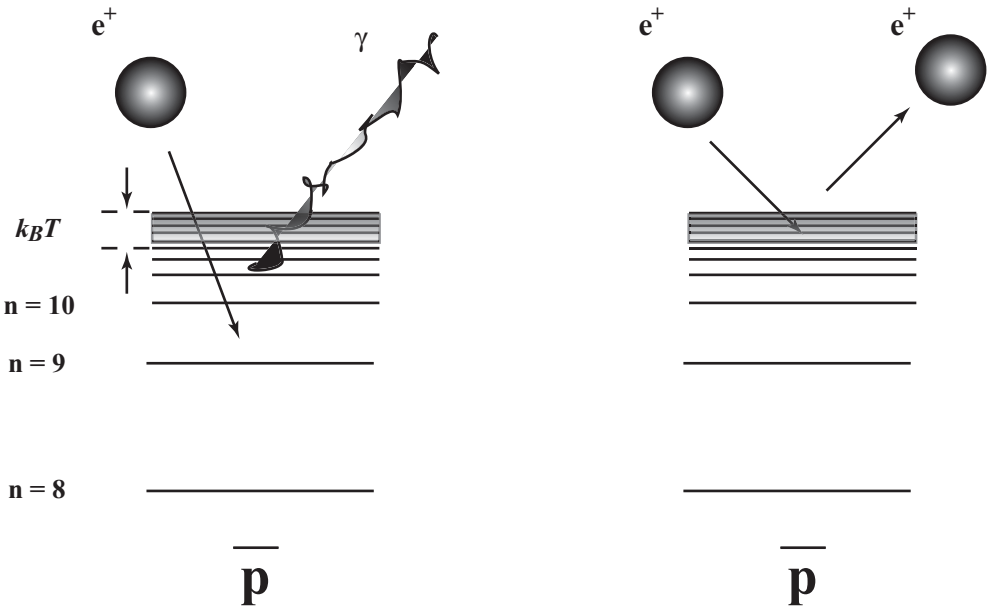

Figure 4.1: Antihydrogen production process. Two-body radiative process (left) and three-body process (right). The photon (positron) carries out the excess energy of the captured positron at the radiative process (three-body process).

4.2 Plasma Manipulation and Diagnosis

Since the positrons are dense enough to be in a plasma state in the ATHENA trap, plasma techniques can be applied for the control of the positrons. The rotating-wall technique can change the plasma shape (density) by the rotational electric field. The plasma mode system can display the positron behavior in real time. The RF heating, which is installed to suppress antihydrogen production by heating up the positrons, can be used as antihydrogen production diagnosis. The detail of each technique is explained in this section.

4.2.1 Test of a Rotating-Wall technique with electrons

Charged particles confined in the Penning trap have a finite lifetime due to scattering with the background neutral gas and with small static field error. Recently several groups have introduced the rotating-wall in order to avoid these kinds of instabilities [30, 31, 32, 33, 34]. The rotating electric field applied to the split electrodes can make compression effect on the plasma cloud and suppress expansion loss in the radial direction (Fig. 4.2). In order to see if this technique can be used to manipulate the particles trapped in the ATHENA trap, we made a test experiment with electrons.

Under the normal conditions (see Sec. 2.2.2), the electron life time is nearly infinite, thus we intentionally made a poor vacuum condition of 10^{-9} mbar (measured by the external vacuum gauge). The electrons are trapped into the harmonic well, are applied the rotating wall for 60 s and are dumped to the Faraday-cup to count the number. The result is shown in Fig. 4.3. As the graph shows, the electron lifetime becomes longer by the rotating-wall compression effect even in the bad vacuum condition.

4.2.2 Determination of the plasma shape using the plasma mode system

The plasma mode system developed and installed in the ATHENA experiment, can be used to determine the plasma shape (and density) using the method described here.

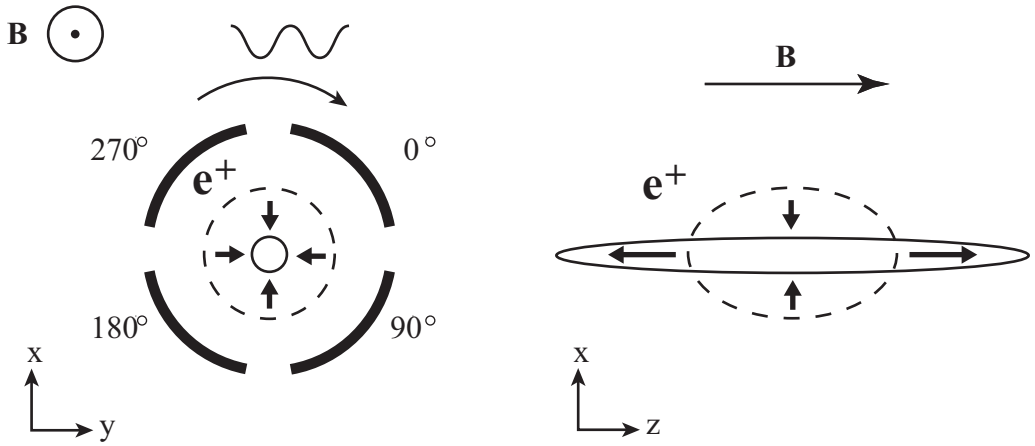

Figure 4.2: Schematic diagram of the rotating-wall method. The voltage of sine-wave function is applied to the split electrodes, and the phase of each sine-wave being shifted by 90° to make rotation electric field (left figure). The plasma is compressed in radial direction and the cloud becomes longer in axial direction (right figure).

Theoretical model

Recently a theory has been developed in the cold fluid limit of plasma where correlations between particles are neglected [35, 36]. In order to be able to apply this theory, the following conditions need to be satisfied:

1. Plasma is cold enough so that its density is uniform.
2. Plasma has a spheroidal shape.
3. Plasma is confined by an exactly quadratic potential. In a cylindrical coordinate (ρ, θ, z), the potential can be written as

$$\phi(\rho, z) = -V\frac{\rho^2 - 2z^2}{2L^2 + b^2}, \tag{4.3}$$

where L is distance from the center of harmonic well to the end cap, and b is trap radius.

Our trap system seems to satisfy these conditions.

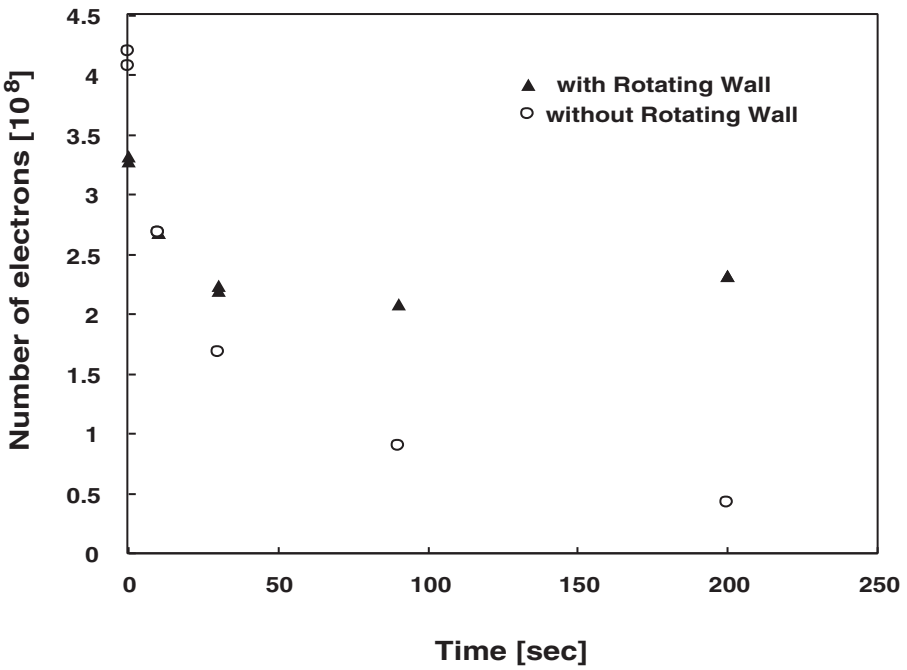

Figure 4.3: Electron lifetimes with and without compression by the rotating-wall. The data were intentionally taken with a poor vacuum condition ($\sim 10^{-9}$ mbar). The lifetime is longer when compressed by the rotating-wall.

To express the plasma shape, we introduce the 'aspect ratio' $\alpha = z_p/2\rho_p$ where z_p and ρ_p are plasma length and radius respectively. For a prolate spheroid, i.e., $\alpha > 1$, the plasma density $n(\alpha)$ can be written as,

$$n(\alpha) = \frac{2V}{\pi e(2L^2 + b^2)\beta(\alpha)}, \tag{4.4}$$

$$\beta(\alpha) = -\frac{2(\frac{1}{\alpha})^2}{1-(\frac{1}{\alpha})^2} + \frac{(\frac{1}{\alpha})^2}{\{1-(\frac{1}{\alpha})^2\}^{3/2}} \log\left|\frac{1+\sqrt{1-(\frac{1}{\alpha})^2}}{1-\sqrt{1-(\frac{1}{\alpha})^2}}\right|, \tag{4.5}$$

and then plasma radius ρ_p can be,

$$\rho_p(\alpha) = \left(\frac{3N}{4\pi n(\alpha)\alpha}\right)^{1/3}, \tag{4.6}$$

where N is total number of particles [37, 38].

We look at some of typical frequencies which is needed for the below discussion; the plasma frequency is defined by $\omega_p = (4\pi n(\alpha)e^2/m)^{1/2}$ and the cyclotron frequency is defined by $\Omega_c = eB/mc$, where e and m are charge and mass of the trapped particles, and c is the speed of light. The plasma axial motion (the dipole mode) is defined by

$$\omega_z = \sqrt{\frac{4eVC_2}{m(2L^2 + b^2)}}, \tag{4.7}$$

here C_2 is a geometrical factor determined by trap geometry. For strongly magnetized plasma ($\omega_p \gg \Omega_c$), the cold fluid dispersion relation is approximated by [39]

$$\epsilon_3 - \frac{k_2}{k_1}\frac{P_l(k_1)Q_l'(k_2)}{P_l'(k_1)Q_l(k_2)} = 0. \tag{4.8}$$

Here, $k_1 = \alpha(\alpha^2 - \epsilon_3)^{-1/2}$, $k_2 = \alpha(\alpha^2 - 3/2)^{-1/2}$, and $\epsilon_3 = 1 - \omega_p^2/\omega^2$. P_l and Q_l are Legendre functions of the first and second kinds, and l is azimuthal quantum number. Eq. 4.8 with $l = 2$ gives us the quadrupole mode frequency as the solution of ω (ω with $l = 1(2)$ corresponds the dipole (quadrupole)

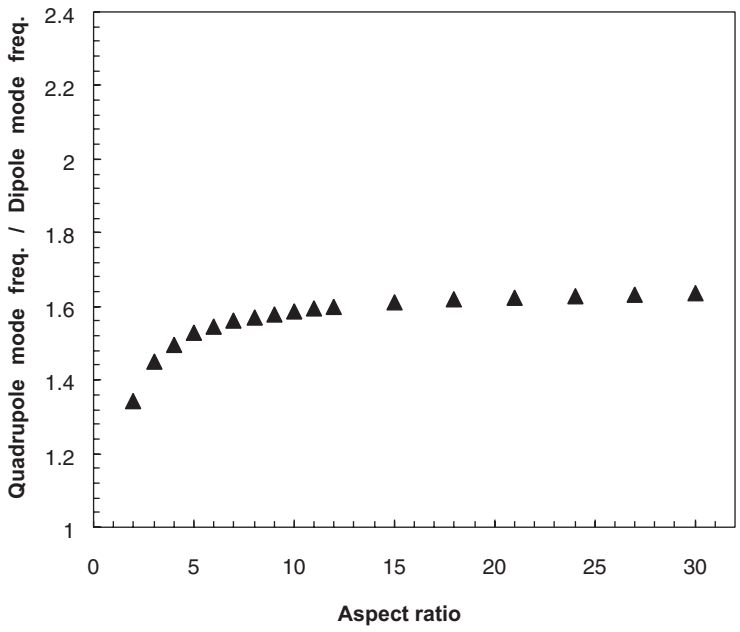

Figure 4.4: The relationship between the mode frequencies and the indicated aspect ratio. The reliable range is with the aspect ratio of $\sim 3-\sim 25$. Beyond this range the reliability of values indicated from the mode system becomes low.

mode frequency.). The solution to Eq. 4.8 can be expressed as function of α only. Fig. 4.4 shows the aspect ratio dependence of plasma mode frequencies. The graph shows that it is hard to estimate the aspect ratio precisely if the aspect ratio is below ~ 3 or above ~ 25.

4.3 Compression and expansion of the positron plasma using the rotating-wall technique

We now discuss the method to modify the positron density using the rotating-wall technique. The shape of the positron cloud is changed by applying a rotational electric field, and its aspect ratio is monitored by measuring the plasma mode frequencies. This sequence was inserted before each positron-antiproton mixing cycle.

Usually the rotating-wall requires about 100 s for plasma compression. But to insert the rotating-wall sequence to the antihydrogen production cycle requires a much shorter time of some 26 s.

In this section, the details of rotating-wall optimization for faster and more precise manipulation with the help of non-destructive monitoring achieved by the plasma mode system are described.

As shown in Fig. 4.5, positrons transferred from its accumulating system are located at the center of the nested trap, which consists of the 5 electrodes, R16 − 20. The rotating-wall RF source is connected to the split-electrode R19 and the plasma mode system is connected to R17. The waveform generator (DS 345; SRS, USA) is connected to R17 as RF field source for positron heating.

To make the rotating electric field, the wave function generator (1946, NF corporation, Japan) is used. This module has two-channel outputs, the phase shift between which can be controlled. The detail of the specification and setup parameters for the measurement are summarized in Tab. 4.2.

The four sine-wave voltages with a phase difference of 90° each (0°, 90°, 180° and 270°) are generated by the waveform generator and the phase splitter. The phase splitter makes two outputs with 0° and 180° phase shift against input. Two sine waves with the phase of 0° and 90° from the waveform generator become 0°, 90°, 180° and 270° through the phase splitter, and they are applied to the four segmented electrodes (as shown in Fig. 4.5)

4.3.1 Optimization

We searched for the optimum parameters (frequency, amplitude and sweep frequency range) in the following way:

1. Search for the plasma compression resonance frequency.
2. Cross check with the destructive method.
3. Optimize sweep condition.
4. Search for other resonance.
5. Amplitude optimization.

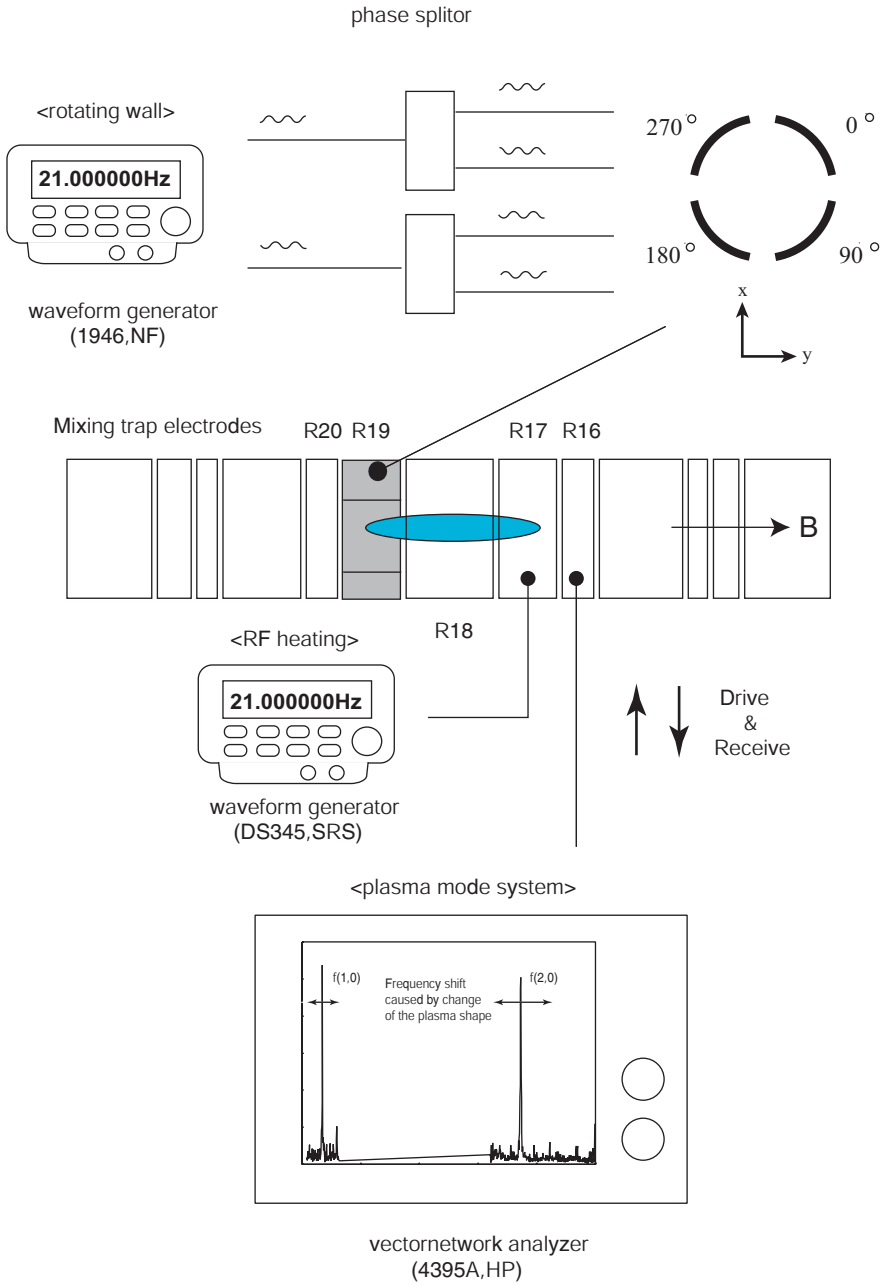

Figure 4.5: Schematic picture of rotating-wall setup. The region of R16 – 20 is the central part of the nested trap. The split electrode R19 is connected to the rotating-wall modules, R17 is connected to the RF heating module, and R16 is connected to the plasma mode system.

Output waveform(sine wave)	
Waveform vertical resolution	12 bit
Frequency range	$0.01\,\mu$Hz to 15 MHz
Frequency setting resolution	$0.01\,\mu$Hz
Frequency accuracy	± 5 ppm
Output voltage	
Amplitude setting range	$0\,\mathrm{mV_{p-p}}$ to $20\,\mathrm{V_{p-p}}$
Amplitude accuracy	$\pm 2\,\%$ of $\mathrm{V_{p-p}}$
Output impedance	$50\,\Omega \pm 2\,\%$
Sweep function	
Sweep items	frequency and amplitude
Sweeping time	1 ms to 10000.000 s
Sweep trigger	indicates start of sweep
Trigger source	external trigger
Trigger delay	$2\,\mathrm{ms} \pm 1\,\mathrm{s}$
Channel operation	
Difference between channels	same waveform, < 10 ns time difference
Phase	common 90° with trigger sweep
Phase setting resolution	0.001°

Table 4.2: The specification of the wave function generator (NF1946).

Search for the plasma compression resonance frequency

One resonance frequency of the rotating-wall was found by the destructive method. The rotating-wall with 1 V amplitude was applied to electrons for 60 s and the only central part of electrons along to the magnetic field were dumped to the Faraday-cup, which is set at one side of the trap system, by two steps potential dump as shown in Fig. 4.6. In general, the particles are released from the central part by the dump because the potential used for confinement is the smallest on axis. The potential height of the first dump is set so chosen that only the central part of the cloud are released and the rest part is released at the second dump. The result is shown in Fig. 4.7, where the number of electrons counted by the Faraday-cup versus applied frequency is presented. We see an increase of the electron number at around 3 MHz when the rotation direction is clockwise[1] indicating that the plasma was radially compressed by the rotating-wall. When the rotation direction was reversed, no compression was observed.

Cross check with the destructive method

The resonance found in the destructive method was studied by the plasma mode system, in order to assess the reliability of the latter. The rotating-wall is applied from $50 - 150$ s after the positron transfer. During 200 s trapping time, the positron behavior is monitored with the plasma mode system. The rotating-wall parameters are 1 V amplitude, 100 s duration time, and $2.5 - 3.5$ MHz sweeping frequency range.

The two lowest plasma mode without rotating-wall is shown in Fig. 4.8**a** and the aspect ratio inferred from these two frequencies is in Fig. 4.8**b**. As graph shows, there is no change in the dipole mode frequency which expresses the axial oscillation of plasma, and the quadrupole mode frequency is slightly shifted. The aspect ratio also slightly changes, about 10 % smaller after 180 s. This tiny expansion may be caused by the instability of the Penning trap system, and the behavior of the frequency and the indicated aspect ratio seem reasonable.

The behaviors of positron plasma with application of the rotating-wall are shown in Fig. 4.9. Fig. 4.9**a** and **b** are the behavior of the frequencies with clockwise rotation (CW) and counter-clockwise rotation (CCW), respectively

[1]This phase direction of the rotating-wall is the same direction of the plasma rigid-rotor, which is determined by the trap system ($\vec{E} \times \vec{B}$).

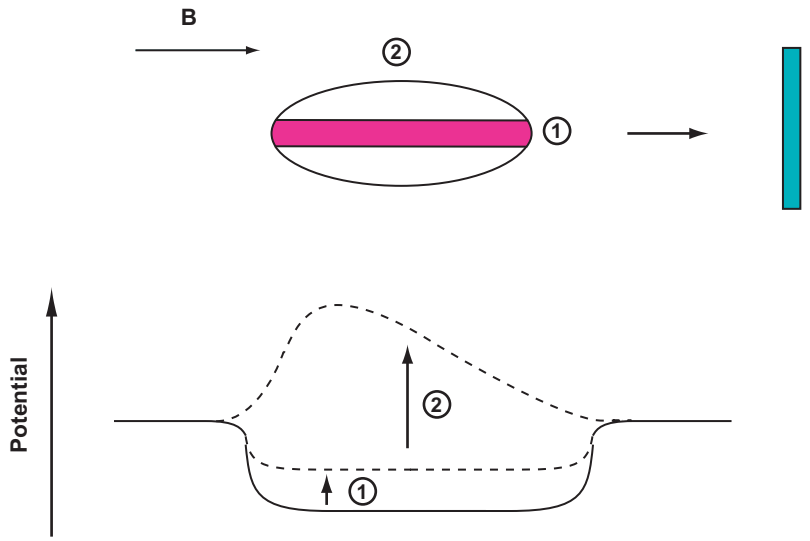

Figure 4.6: The schematic picture of counting the central part of the electron cloud. In general, the confined electrons are released from on axis by the dump. The dump is consisted of two steps (top figure), and the central part of the cloud are released at the first step and the rest part are at the second step (bottom figure).

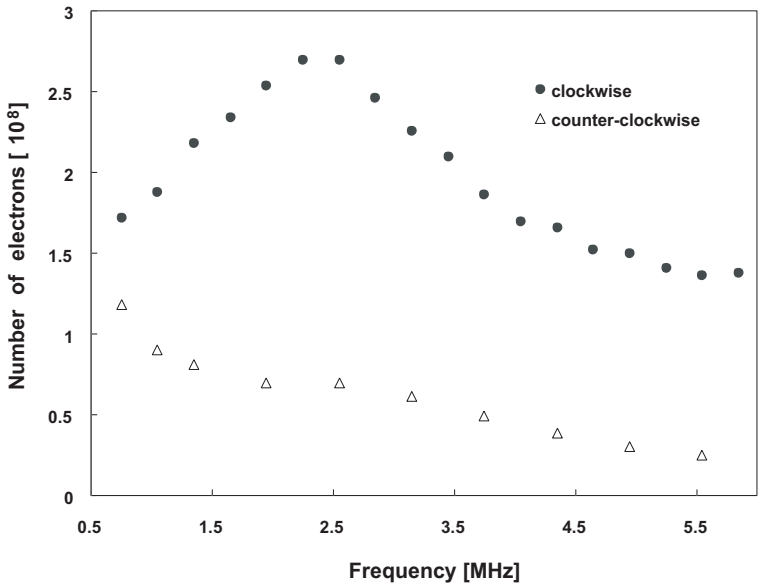

Figure 4.7: The resonance of the rotating-wall frequency at around 3 MHz for electrons. The graph shows the electron number in the central part of the cloud versus the applied rotating-wall frequency (see text). The numbers of electrons are counted by the destructive way. Only for one direction the numbers go up at the frequency of around 3 MHz, and this effect means compression of the cloud.

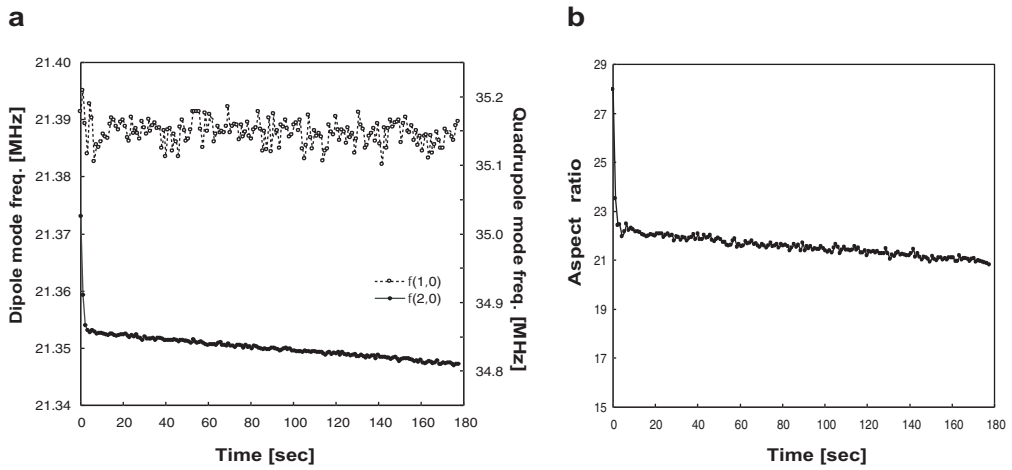

Figure 4.8: The positron plasma behavior observed with the plasma mode system. **a,** Typical behaviors of plasma mode frequencies. The dipole mode frequency seems no changes and the quadrupole mode frequency is slightly shifted to lower side. **b,** The aspect ratio deduced from the mode frequencies applying the cold fluid theory. The positron plasma is found to expand by about 10% after 180 s trapping time.

and Fig. 4.9**c** and **d** are corresponding aspect ratio values. As graphs show, when rotating-wall is turned on $t = 50$ s the quadrupole mode frequency suddenly jumps up (meanwhile the dipole mode frequency is almost stable). Since the quadrupole mode frequency contains the temperature information, this means that positrons are heated up by the rotating-wall. The quadrupole mode frequency goes down at the and of the rotating-wall (150 s) cooling by synchrotron radiation, but dose not come back to the same frequency. As shown in Fig. 4.9**c**, when the rotation direction is clockwise, the aspect ratio is larger after the rotating-wall is applied. It means that the plasma is compressed and is consistent with the result obtained by the distractive measurement. Fig. 4.9**d** shows, in contrast, that the plasma is expanded. We can therefore manipulate the plasma aspect ratio (and hence its density) by using the rotating-wall method.

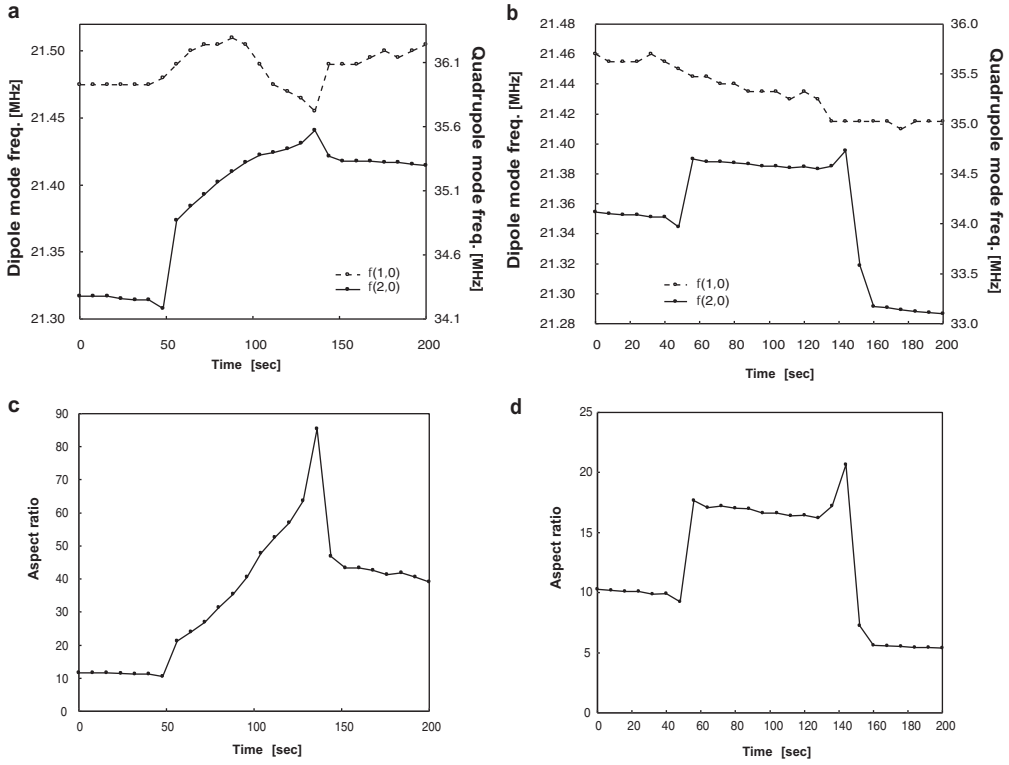

Figure 4.9: The typical behaviors of positron plasma with application of the rotating-wall at around 3 MHz. **a,** The behaviors of the frequencies for compression. **b,** The behaviors of the frequencies for expansion. **c,** The deduced aspect ratio for compression. The ratio goes up from about 10 to 40 by the rotating-wall. **d,** The indicated aspect ratio for expansion. The ratio goes down from about 10 to 5 by rotating-wall. The rotating-wall conditions are, amplitude of 1 V and sweep with $2.5 - 3.5$ MHz for 100 s. The duration period is $50 - 150$ s in the graphs.

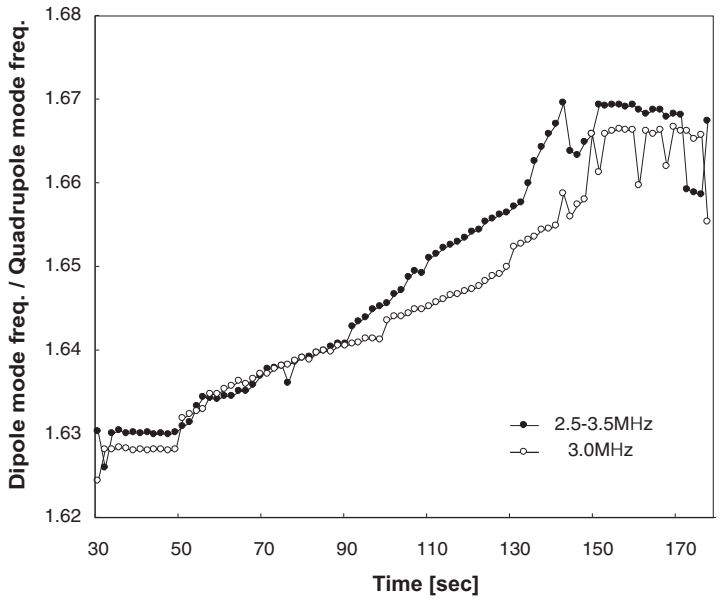

Figure 4.10: The difference of rotating-wall effects between swept and fixed frequencies. The rotating-wall conditions are, amplitude of 1 V and sweep with $2.5 - 3.5$ MHz or 3.0 MHz for 100 s. The duration period is $50 - 150$ s in the graphs. The effect looks slightly better wtih the swept frequency than the fixed frequency. Hence to sweep the applied frequency can take advantage for covering the resonance frequency.

Sweep condition

The observed rotating-wall resonance is broad ($\sim$ 1 MHZ) as shown in Fig. 4.7. We compare two cases, one with a fixed-frequency wall (3 MHz) and the other with a variable-frequency wall (sweep from 2.5 MHz to 3.5 MHz over the 100 s), in order to see which method is more effective to manipulate the plasma.

The result is shown in Fig. 4.10. The effect looks slightly better with the variable-frequency than the fixed-frequency. The reason may be that the resonance is shifted as the plasma shape is changed by the rotating-wall [47]. To sweep the applied frequency can take advantage for covering the resonance frequency if it is shifted (from lower to higher frequency in the compression case).

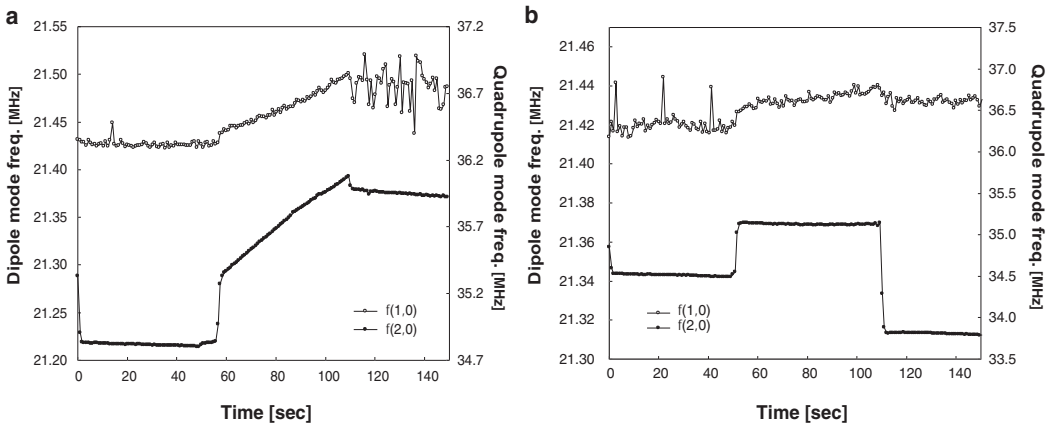

Figure 4.11: The typical behaviors of positron plasma with application of the rotating-wall at around 6 MHz. The rotating-wall conditions are, amplitude of 1 V and sweep with $6.7 - 7.0$ MHz for 60 s. The duration period is $50 - 110$ s in the graphs. **a,** The behaviors of the mode frequenceis for compression. **b,** The behaviors of the mode frequencies for expansion.

Search for other resonance

Frequency survey is done with 100 KHz step from $0 - 10$ MHz (the rotating-wall duration time is 60 s for each step). Compression effects were observed at two frequency ranges, $2.5 - 3.5$ MHz and $6.7 - 7.0$ MHz.

The behaviors of mode frequencies of the 6 MHz resonance is shown in Fig. 4.11. They are similar to the 3 MHz resonance. In the CW direction, the plasma is compressed and the plasma expands in the CCW direction.

In order to find out which of the two resonance is more effective for plasma manipulation, we compare the ratio the dipole mode frequency/the quadrapole mode frequency for both resonance in Fig. 4.12. The ratio of the dipole mode frequency/the quadrapole mode frequency quickly goes up in around 6 MHz, when the rotating-wall is applied, and after the rotating-wall, the ratio is changed more at 6 MHz than at 3 MHz.

It means that the rotating-wall at the resonance around 6 MHz is more effective for plasma compression (or expansion).

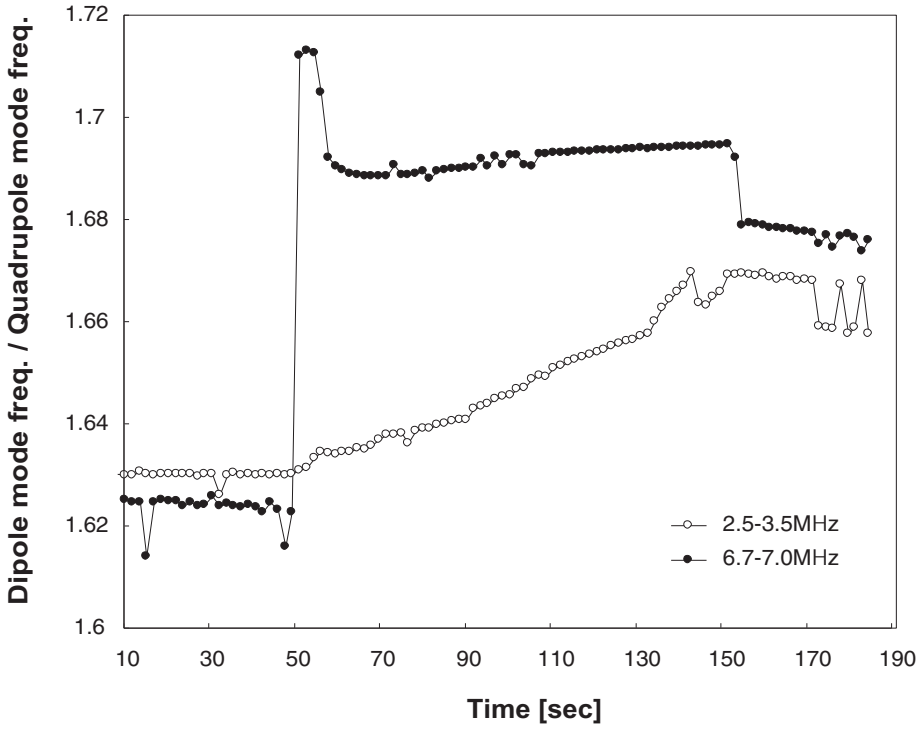

Figure 4.12: The difference in compression effect between the resonance 3 MHz and 6 MHz. The rotating-wall conditions are, amplitude of 1 V and sweep with $2.5 - 3.5$ MHz or $6.7 - 7.0$ MHz for 100 s. The duration period is $50 - 150$ s in the graphs. The effect seems better for the resonance around 6 MHz.

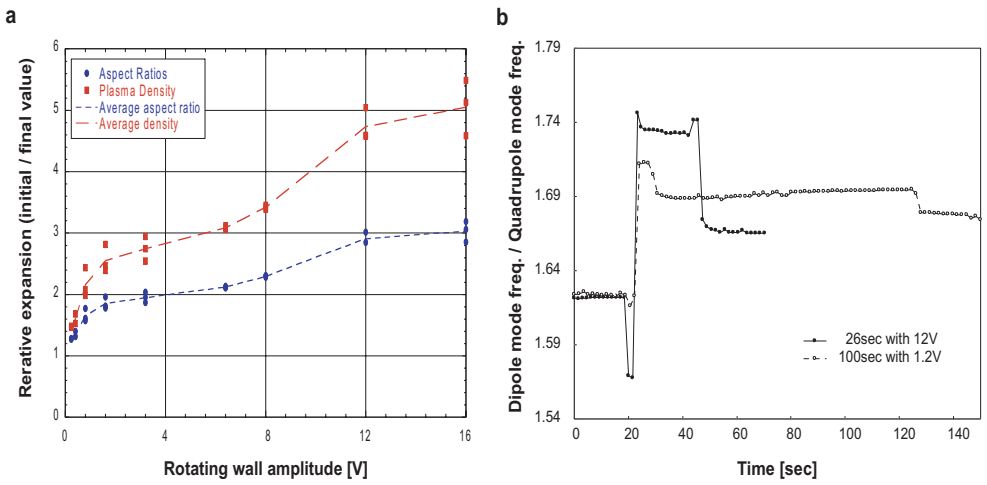

Figure 4.13: Amplitude optimization. **a,** The amplitude survey for expansion direction. As the amplitude is bigger, the effect seems to become better. **b,** The compression effects the 26 s-wall with 12 V and the 100 s-wall with 1.2 V (see text). Compression effects seem similar in the both cases.

Amplitude optimization

The survey of the amplitude was done for the 6 MHz resonance. The rotating-wall frequency was swept from 6.7 MHz to 7 MHz over 100 s. The phase direction is set for expansion because it is easy to see the effect. The result is shown in Fig. 4.13**a**; the larger amplitude seems to be more effective.

We then set amplitude at 12 V, and tried to shorten the rotating-wall period. As shown in Fig. 4.13**b**, the 26 s-wall with 12 V is as effective as the 100 s-wall with 1.2 V.

Achieved performance

With the help of the plasma mode system, the optimization of the rotating-wall is achieved. We can prepare three different shapes of positrons with the short duration time of 26 s. Parameters of each positrons are summarized on Tab. 4.3.

	α	ρ_p [mm]	$2z_p$ [cm]	n [cm^{-3}]
compression	72	0.3	2.2	7×10^9
no wall	20	1.0	2.0	8×10^8
expansion	6.5	2.5	1.6	1.5×10^8

Table 4.3: The parameters of several different kinds of positron clouds, achieved by the rotating-wall. The table shows the typical values indicated from the plasma mode system.

4.4 Study of antihydrogen production mechanism using the rotating-wall

The optimized rotating-wall can be incorporated to the antihydrogen production cycle. Rotating wall duration time (26 s) is inserted before the injection of antiprotons, and prepare the three different shapes of positrons. We check the differences of antihydrogen production behaviors between these three clouds by using the silicon detector.

4.4.1 Effect of plasma compression (expansion) on the formation rate

During the mixing cycle, positrons are accumulated and transferred to the center of the nested trap and antiprotons are captured in the catching trap and move to the location next to the nested trap at the mixing trap. Before the antiproton injection, we applied the rotating-wall to the positron cloud and wait more than 10 s to cool back again. After the injection, the behaviors are observed by the silicon strip detector and the plasma mode system during the 60 s mixing cycle. We repeat this cycle for three different shapes of positrons, compression ($\alpha \sim 80$), no wall ($\alpha \sim 20$) and expansion ($\alpha \sim 7$) (Tab. 4.3), and take the statistics for each positrons.

The results of antiproton annihilation signals as seen by the silicon detector for compression, no wall, and expansion are shown in Fig. 4.14. The detector is off for the first 1 s (called 'time cut'). The numbers of data acquisition cycles for different shapes are; the compression 7 cycles, no wall 17 cycles, and the expansion 44 cycles. We can see a clear difference between these cases.

Without rotating-wall, antiproton annihilations decrease with time and two components can be seen in the annihilation time spectrum, a 'prompt peak' and a 'slow tail'. The prompt peak appears just after injection of antiprotons and the slow tail appears later with a time constant of 10 s. In the case of compression, the prompt peak raises higher than that of no wall, and the new second peak appears several seconds after the start of the mixing. In the case of expansion, the prompt peak disappears and only the slow tail can be seen. But the height of the tail becomes higher.

Subsequently, the annihilation time spectra were measured with RF heating applied to the positrons. If the antiproton annihilations come from the antihydrogen atoms, the signals on the silicon detector should disappear due to suppression of the antihydrogen production. The results are shown in Fig. 4.15. As graphs show, the almost all the triggers decrease, and the second peak at compression also disappears.

4.4.2 Efficiency of antiproton cooling with different positron shape

For the study of the density dependence for antihydrogen production more carefully, we try to understand cooling efficiency with different shapes of positrons. During the mixing, an antiproton has interaction with positrons many times, and forms antihydrogen when their relative velocity becomes low enough. It means that the positrons with the best cooling efficiency is expected to give us the most antihydrogen. We try to measure the cooling efficiency by observing the antiproton energy after the mixing.

We set a short mixing time of 100 ms, after which the antiprotons are slowly released in the three steps as shown in Fig. 4.16**b**.

In step 1, LW is lowered to the same level as e^+W for releasing the hot part of antiprotons in the whole well.

In step 2, the bottom part of LW is raised to dump the cold part of antiprotons in LW.

In step 3, RW is raised to release the cold part of antiprotons in RW.

The result is shown in Fig. 4.16**a**. The graphs show antiproton annihilation time-spectra for compression, no wall and expansion from top to bottom. The separated sections marked with numbers in Fig. 4.16**a** corresponds to

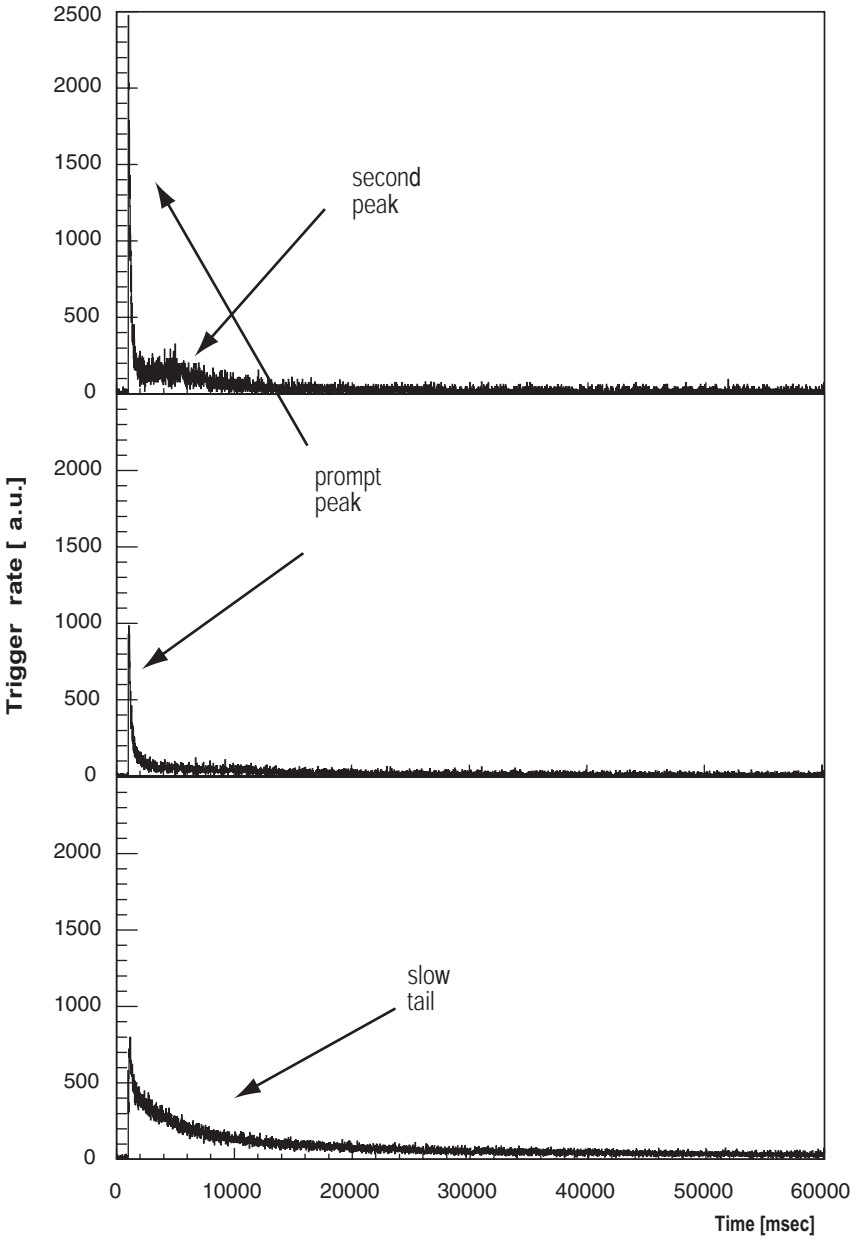

Figure 4.14: Trigger rates during the mixing with the different shapes of positron clouds. From top to bottom, 'compression', 'no wall' and 'expansion'. Each graph shows different behavior.

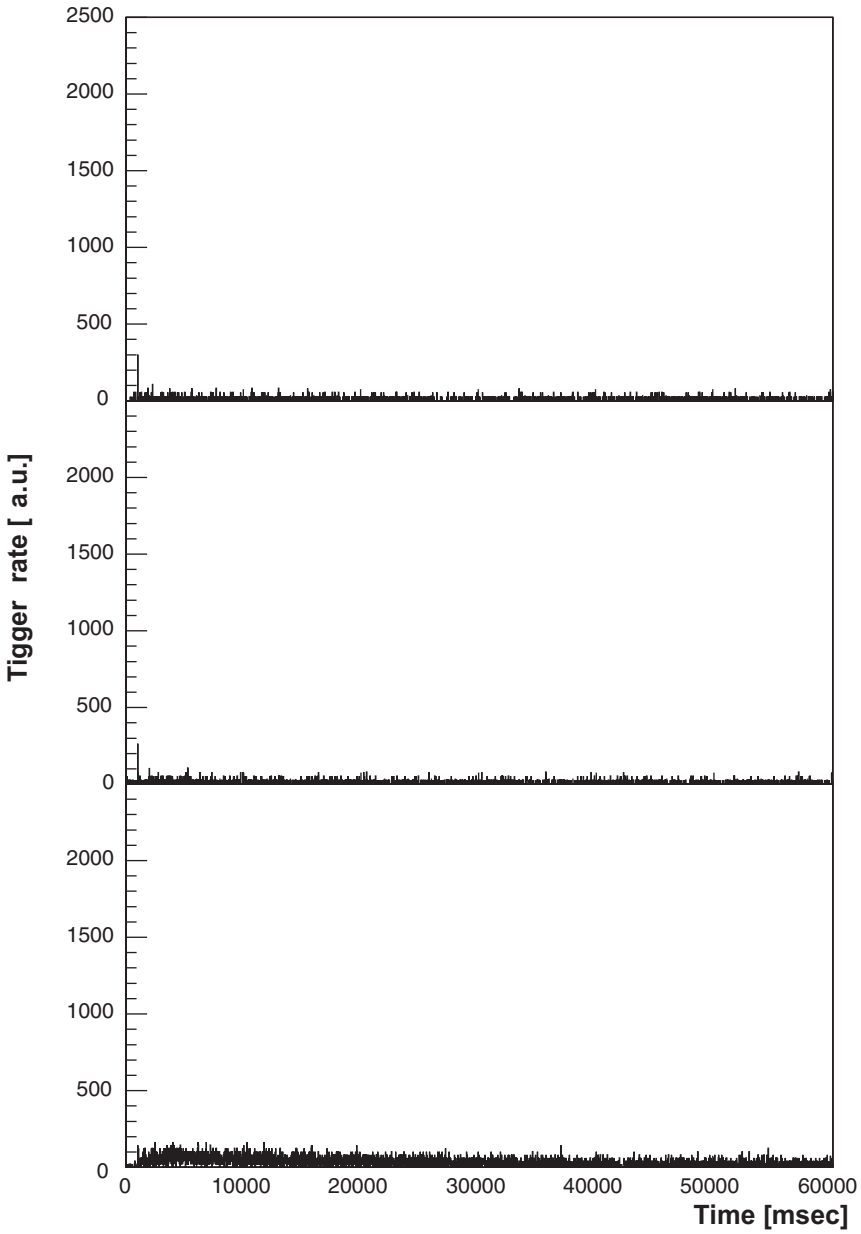

Figure 4.15: Trigger rates with application of RF heating for different positron plasmas. The RF heating is applied during the mixing. The data are 'compression', 'no wall' and 'expansion' from top to bottom. The triggers drastically decrease in all the case, and the second peak at compression also disappears.

	step 1	step 2	step 3	total
compression	704 (80.1 %)	147 (16.7 %)	28 (3.2 %)	879 (100 %)
no wall	668 (66.9 %)	270 (27.0 %)	61 (6.1 %)	999 (100 %)
expansion	435 (36.8 %)	639 (54.0 %)	109 (9.2 %)	1183 (100 %)

Table 4.4: The number of triggers in the energy measurement. Each step corresponds to the section marked in in Fig. 4.16.

the dump steps shown in Fig. 4.16**b**. And the numbers of triggers counted in the each step are on Tab. 4.4.

As Tab. 4.4 shows, the number of antiprotons at the bottom of LW (which corresponds 'step 2' on Tab. 4.4) goes up as the radius of positrons increases. It means that the expanded plasma has the best cooling efficiency even if it has the lowest density, and the compressed plasma has the worst. This may be due to differences in overlap time of two species which come from the interaction dynamics. In our system, we can indicate some reasons. There is a misalignment between the magnetic field and the center line of the trap system, and additinally the electric potential depends on the radial position in the nested trap (see Fig. 4.17). If so, the motions of charged particles become complicated, unlike going back and force along the center axis. Thus the positron plasma with the larger radius can easily overlap with the antiprotons.

Aother suport, simulation taking the ATHENA setup into consideration, is needed for further progress in understanding the complete dynamics of antiprotons and positrons interaction mechnism.

4.4.3 Discussion

In the energy measurement, the expanded plasma has the best cooling efficiency. But it dose not mean higher antihydrogen production rate. In Fig. 4.14, we overlay the annihilation rates measured with the silicon detector (a good indicator of antihydrogen formation rate) for the three plasma shapes. Fig. 4.18**a** shows the first 20 s of the mixing and the Fig. 4.18**b** is focused on the first 2 s.

The temperatures of all the cases should be same because the cooling time (10 s) which is enough for the synchrotron radiation is prepared before the mixing. The prompt peak disappears in the case of 'expansion', and the

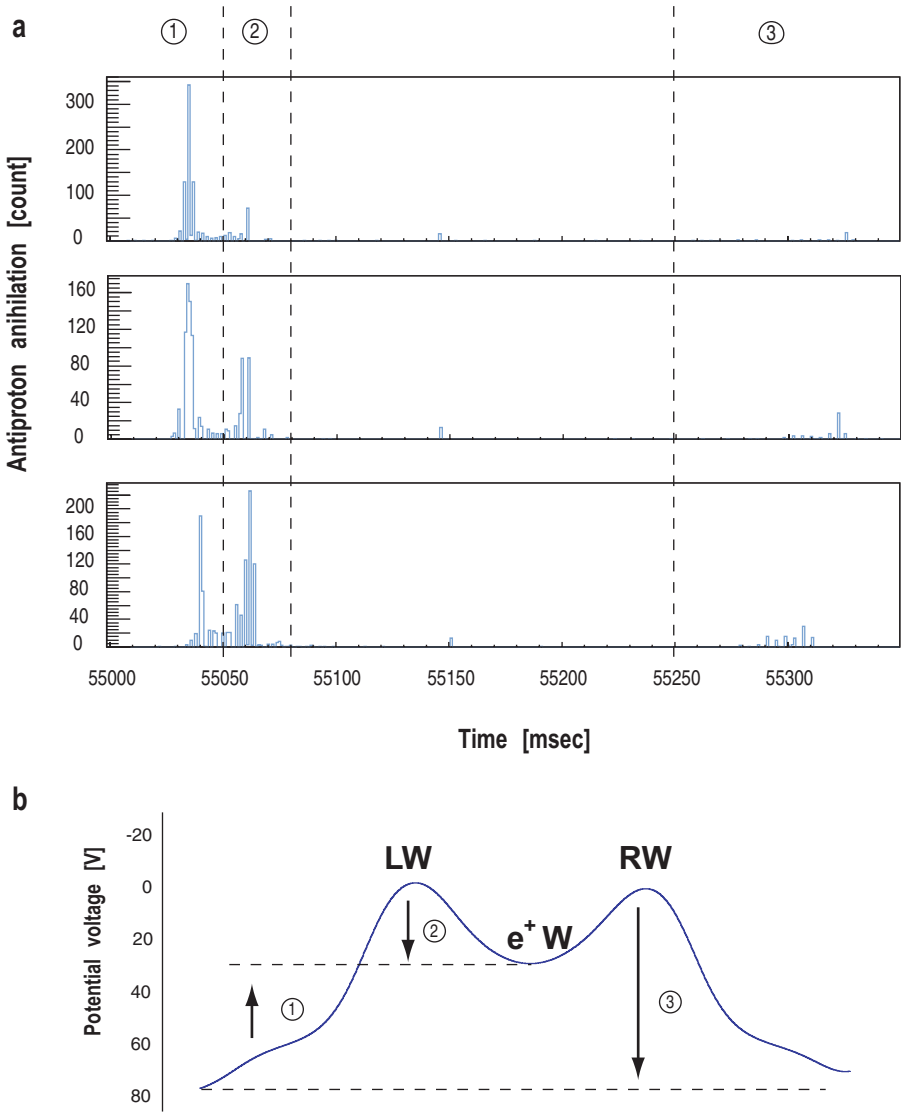

Figure 4.16: Positron plasma cooling efficiency with different shapes. **a,** Time spectrum of the antiproton annihilation signals dumped after 100 ms mixing. From top to bottom, graphs are 'compression', 'no wall' and 'expansion'. The signals are counted by the external scintillators. **b,** The three steps potential dump procedure. All the antiprotons are released in three steps. The First step starts 100 ms after mixing. The numbers correspond with each other in both figures.

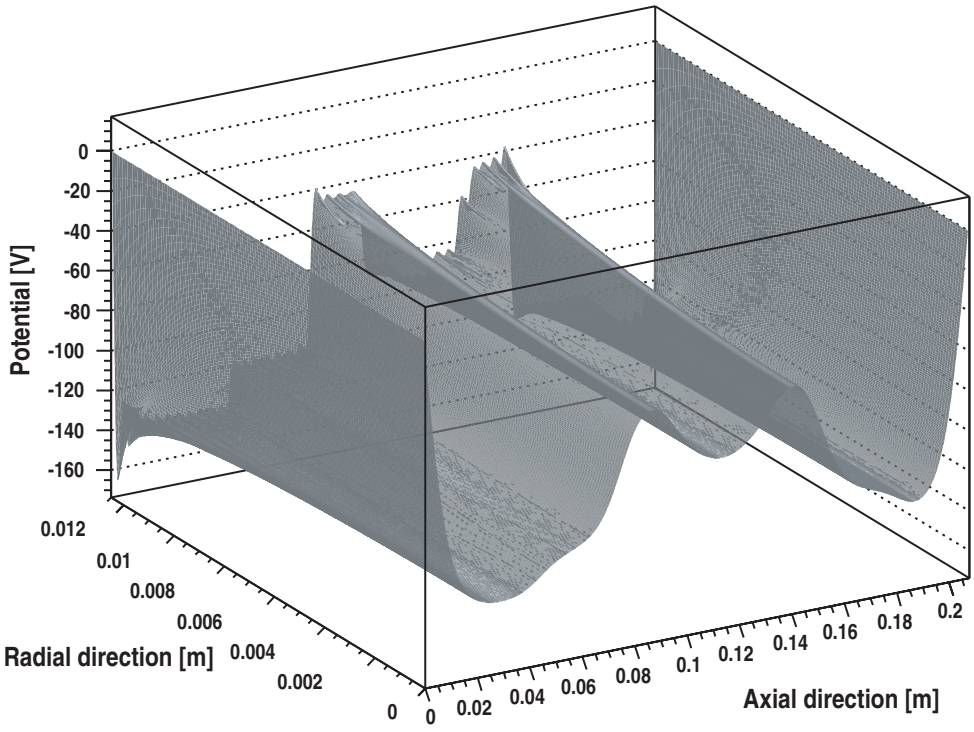

Figure 4.17: The three-dimensional potential shape of the nested trap. Further from the center axis, the actual potential is changed from that on axis like as the surface of wave function in the figure.

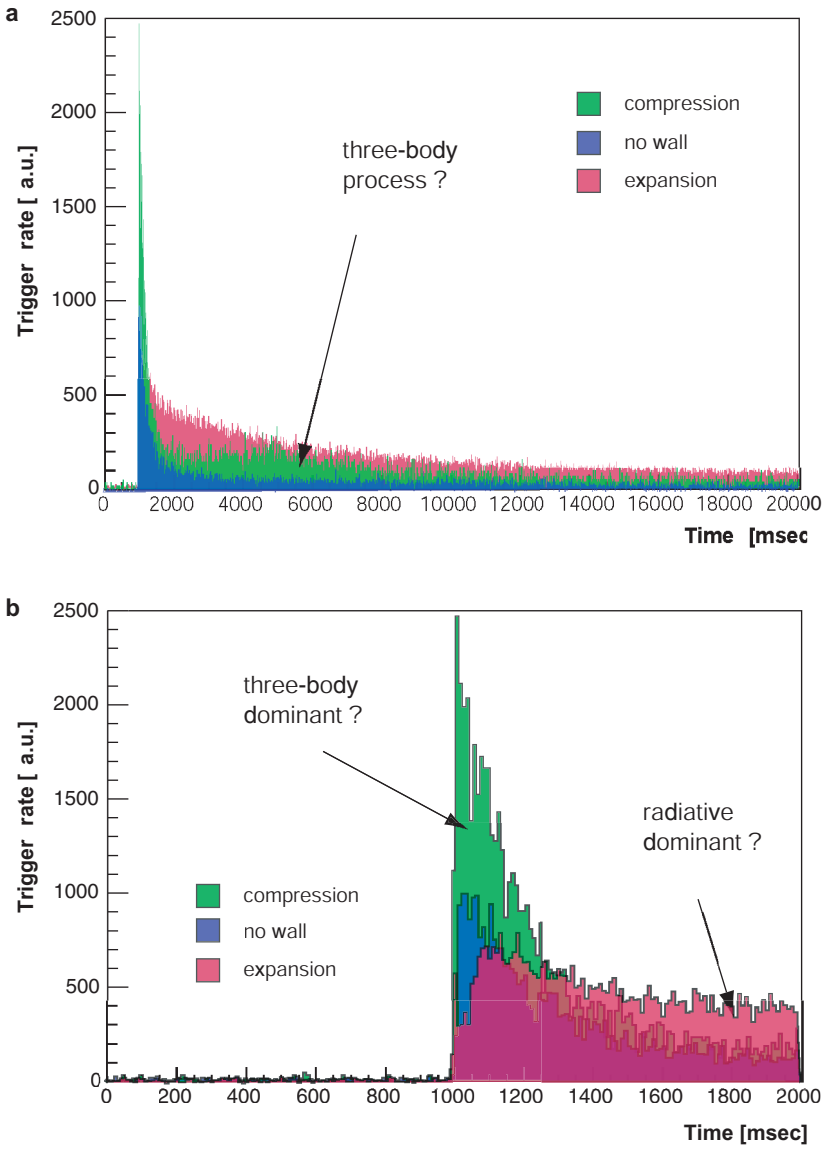

Figure 4.18: The trigger behaviors with the different shapes of positron clouds. The background of green, blue, and pink correspond to 'compression', 'no wall' and 'expansion', respectively. **a,** Triggers in the first 20 s of the mixing. **b,** Triggers in the first 2 s of the mixing. Time cut is applied for the first 1 s.

second peak appears only in the case of 'compression'. The slow tail goes up as the density of the cloud decreased. With RF-heating, additionally, we can notice that the number of triggers certainly decrease in all the cases, but they still remain slightly bigger in the case of 'expansion' than the other cases. These differences present the temperature dependence on antihydrogen production processes. We can predict that the antihydrogen atoms are produced by not only one process because the triggers should decrease with the same way if the antihydrogen atoms are produced by the same process. Since the three-body process depends on the positron density more strongly than the radiative process, we assume that the three-body process is dominant in dense positron cloud and the radiative process is dominant in less dense cloud.

If (the three-body process is killed and) the radiative process is dominant in the case of 'expansion', and (the radiative process is killed and) the three-body process is dominant in the case of 'compression', we can predict the following; reconstruction

1. The three-body process is dominant in the prompt peak.
2. The radiative process is dominant in the slow tail.
3. The second peak comes from the three-body process.

Another confirmation for the first issue can be seen at the differences in the prompt peak for 'compression' and 'no wall'. The peak height increases proportional to the density, this fact is consistent with the theory.

4.5 To the laser experiment

The unique plasma control by the rotating-wall has performed the density dependence of the antihydrogen production study for the first time. We noticed that the antihydrogen atom production mechanism becomes so complicated because of some difficulties in the ATHENA instruments, such as the magnetic field, and theoretical guidance and the simulation of the dynamics of antiprotons and positrons combination process are certainly needed to for further progress in understanding.

This technique can also be used in the next laser experiment. One of the most important usages is control of the antihydrogen production process. The

two production mechanisms lead to different quantum state populations of produced antiatoms. Therefore selection of these processes by the change of positron shape enables to prepare the required state, $n < 10$ in the radiative process and $n \gg 10$ in the three-body process.

The understanding and controlling these complex processes will completely be achieved in near future, and the laser spectroscopy with antihydrogen atoms is now within experimental reach.

Chapter 5

Summary

The ATHENA experiment succeeded in producing large amounts of cold antihydrogen in the year 2002 at CERN. This is a milestone for the study of antimatter, and the integration of a laser spectroscopy experiment (which may lead to high precision tests of CPT) is expected as a next step.

Antihydrogen production is achieved by mixing large amounts of antiprotons and positrons in a nested Penning trap. The antihydrogen annihilation event is identified from the signals detected during mixing.

The ATHENA instrument is mainly composed of four sections: 1) antiproton catching trap, 2) positron accumulator, 3) mixing trap and 4) antihydrogen detector. To make antihydrogen, a Penning trap system is introduced and adapted to the ATHENA experiment. The apparatus is composed of a sequence of cylindrical rings and is suited for the confinement of a large amount of charged particles by electromagnetic fields. For the special purpose of trapping antiparticles, the trap systems are housed in the bore of a 3 T superconducting magnet, inside which the conditions are kept at cryogenic temperature and ultra high vacuum. A special detector designed to select the antihydrogen events is also built, and mounted very near to the trap system and covers the whole mixing region. The traps and the detector are physically separated because of thermal and pressure problems.

The low energy antiproton beam, which contains 2×10^7 antiprotons with an energy of 5.3 MeV, is provide by the AD; the antiprotons are captured by the high voltages applied to the end cap of the antiproton catching trap, are cooled by application of an electron cooling procedure and are trapped. Finally more than 10^4 antiprotons are confined with energies of the order of

eV per AD shot. Positrons from a radioactive source (1.4 GBq) are cooled and accumulated in the positron accumulator, and then transferred to the mixing trap. 150 million positrons are successfully transferred to the mixing region after 200 s of accumulation. Inside of the trap (since the positron particles are dense enough to be in a plasma state) their complicated behaviors are nondestructively monitored by using plasma techniques, which determine plasma properties from its characteristic oscillations.

Antiprotons are injected into the positron cloud, which is located at the center of the nested potential and mixed for 190 s. During the whole duration of mixing, the detector records data. From the opening angle study, which considers the correlation of two 511 keV photons detected at the same time, the antihydrogen annihilation events can be selected. More than 50000 cold antihydrogen atoms are produced in 165 mixing cycles.

Subsequently further study of antihydrogen atoms is attempted using the plasma control techniques. The processes contributing to production of cold antihydrogen are thought to be the three-body process and the radiative process. In theory, these two processes have different dependencies on positron plasma properties, such as temperature T and density n; $T^{-9/2}$ and n^2 for the three-body process, and $T^{-1/2}$ and n for the radiative process. The plasma manipulation techniques are applied to change positron parameters, and their effect on antihydrogen production are observed on the silicon strip detector.

In the trap experiment, it is not so easy to perform precision control of the trapped charged particles. For example the rotating wall, which can compress the plasma in the radial direction by the rotational electric field and change the plasma shape (density), takes about 100 s. We tried to optimize the rotating wall parameters with the help of the non-destructive plasma display and achieved a much shorter duration of 26 s with precision control. This optimized rotating wall is incorporated into the antihydrogen production cycle. With this duration, three different shapes of positrons are prepared for mixing: compression ($n = 8 \times 10^9\,\mathrm{cm}^{-3}$), no wall ($n = 7 \times 10^8\,\mathrm{cm}^{-3}$) and expansion ($n = 1.5 \times 10^8\,\mathrm{cm}^{-3}$). We use the antiproton annihilation signal on the silicon detector as antihydrogen diagnosis and observe clear differences between these three positron configurations.

For no wall, there are two components, the prompt peak, which appears just after injection of antiprotons, and the slow tail following with a time constant of several seconds. For compression, the prompt peak increases by

about a factor of two compared with no wall, while for expansion, the prompt peak disappears and the slow tail becomes higher. The energy measurement, in which the antiproton energy distribution is measured after mixing, suggests that the cooling efficiency is better in the following order: expansion, no wall, and compression. This means that positrons with bigger radius have better cooling efficiency (lower density) due to the interaction dynamics of antiprotons and positrons in the trap system. The number of antihydrogen atoms, however, does not drastically increase in the case of expansion. This is consistent with a suppression of the three-body process, with only the radiative process remaining. Meanwhile in the case of compression, the three-body process becomes dominant. The prompt peak, which is higher in the case of a denser positron plasma, seems to be due to the three-body process and the slowly declining tail to the radiative process.

The above results deliver hints for understanding the antihydrogen production mechanism and lead to further studies in the near future. These results also include possibility to achieve the controlling the production process, which determine the energy state population of produced antihydrogen atoms. This information is also important for the design of the laser experiment, which is planned as a high precision test of CPT.

Acknowledgments

First of all, my appreciation and thanks are extended to my supervisor Prof. R. S. Hayano, for allowing me the opportunity to participate in an exciting and fulfilling project. I am expecially thankful to our Prof. J. S. Hangst, who organized our collaboration as physics cordinator. Thanks as well to technical cordinator Dr. P. Bowe for letting me play on the appratus as a youngster.

I wish to thank to Italian and Brazilian collaborators; Dr. M. Amoretti, Dr. G. Bonomi, C.Carraro, Dr. A. Fontana, P. Genova, Prof. V. Lagomarsino, Prof. A. Rotondi, Prof. G. Testera, Dr. A. Variola, Prof. E. Lodi-Rizzini N. Zurlo, Prof. G. Manuzio and Prof. C. L. Cesar. They never forget the cheerful atmosphere in the experiment and worked very hard.

Thanks to Prof. M. Charlton, Dr. L. V. Jørgensen, D. Mitchard and Dr. Dirk Peter van der Werf; they developed the one of the best positron source in the world and kept an energetic operation.

Thanks to Dr. M. Doser, Dr. M. Fujiwara Dr. A. Kellerbauer, Dr. R. Landua and Dr. N. Madsen; they staid at CERN and contributed to the experiment as full time workers.

Thanks to Prof. C. Amsler, Dr. I. Johnson Dr. C. Regenfus and J. Rochet; they designed and built the powerful detectors.

Thanks to Dr. A. Bouchta, Dr. K. Fine Dr. M. Holzscheiter D. Lindelof, Dr. M. Marchesotti, Dr. P. Riedler Dr. G. Rouleau and T. L. Watson. They has rendered many services to the experiment.

I would like to express my gratitude for all of the AD crew, who worked very hard to provide us an excellent experimental environment for the study of antimatter science.

I would like to express my sincere thanks to my friends, N. Doshita, Dr. S. Horikawa, M. Jørgensen, Y. Namita, Ricardo, Dr. G. WangDr. N. Takabayashi, H. Tuchiura, Dr. T. Toeda N. Tonomura, T. Yoshizawa. They

helped me so often and made my European life pretty enjoyable. Without their support, I did not continue to my work.

This work was supported by Istituto Nazionale di Fisica Nucleare (Italy), Conselho Nacional de Desenvolvimento Científico e Technológico, Fundaçäo de Amparo a Pesquisa do Estado do Rio de Janeiro (FAPERJ) e Fundaçäo CCMN/UFRJ (Brazil), Grant-in-Aid for Creative Basic Research of Monbukagakusho (Japan), the Swiss National Science Foundation, the Danish Natural Science Research Council, The UK Engineering and Physical Sciences Research Council (EPSRC), The EU (Eurotraps Network), and the Royal Society.

I would like to express my sincere thanks to my two families. Manabu, Junko and Chie Funakoshi; they permitted me to join the ATHENA experiment, and always encouraged me for my selfish dream. Thanks again for their ceaseless support. Takao, Mieko, and Kumiko Yokoyama; they also allow our selfish wishes. I would like to show my special thank for their incredible kind support.

I could finish my writing due to the all of above supports.

Finally, my partner Chieko. She always tried to understand and support me. I dedicate this thesis to her with my greatest appreciation.

Bibliography

[1] M. Niering, R. Holzwarth, J. Reichert, P. Pokasov, Th. Udem, M. Weitz, T. W. Hänsch, P. Lemonde, G. Santarelli, M. Abgrall, P. Laurent, C. Salomon and A. Clairon, Phys. Rev. Lett. **84**, 5496, (2000).

[2] G. Baur *et al.* Phys. Lett. **B 368**, 251, (1996).

[3] G. Blanford *et al.*, Phys. Rev. Lett. **80**,3037, (1998).

[4] R. S. Van Dyck, P. B. Schwinberg and H. G. Dehmelt, Phys. Rev. Lett. **59**, 26, (1987).

[5] G. Gabrielse, X. Fei, L. A. Orozco, R. L. Tjoelker, J. Hans, H. Kalinowsky, J. Hass and W. Kells, Phys. Rev. Lett. **62**, 1360, (1989).

[6] G. Gabrielse, X. Fei, K. Helmerson, S. L. Rolston, R. Tjoelker, T. A. Trainor, H. Kalinowsky, J. Haas and W. Kells, Phys. Rev. Lett. **57**, 2504, (1986).

[7] L. S. Brown and G. Gabrielse, Rev. Mod. Phys. **58**, 233, (1986)

[8] G. Gabrieles, D. Phillips, W. Quint, H. Kalinowsky and G. Rouleau, Phys. Rev. Lett. **74**, 3544, (1995).

[9] G. Gabrielse, X. Fei, L. A. Orozco, R. L. Tjoelker, J. Hans, H. Kalinowsky, J. Hass and W. Kells, Phys. Rev. Lett. **62**, 1360, (1989).

[10] G. Gabrielse, D. Phillips and W. Qunit, Phys. Rev. Lett. **74**, 3544, (1995).

[11] M. Amoretti *et al.* accepted for publication in Nucl. Inst.Meth. Phys. Res. A (2003).

[12] M. H. Holzscheiter *et al*, Phys. At. Nucl., **57**, 1870, (1994).

[13] A. Wolf Hyperfine Interaction **76**, 189, (1993)

[14] M. Amoretti *et al.*, Phys. Plasma **10**, 3056, (2003).

[15] M. Amoretti *et al.*, Phys. Rev. Lett. **91**, 055001-1, (2003).

[16] C. M. Surko, S. J. Gilbert, and R. G. Greaves, in Non-Neutral Plasma Physics III, edited by J. J. Bollinger, R. L. Spencer and R. C. Davidson, AIP Conf. Pro. **498**, 3, (1999)

[17] T. J. Murphy and C. M. Surko, Phys. Rev. A **46**,5696, (1992).

[18] R. G. Greaves, M. D. Tinkle and C. M. Surko, Phys. Plasmas **1**, 1439, (1994).

[19] A. P. Mills Jr. and E. M. Gullikson, Appl. Phys. Lett. **49**, 1121, (1986).

[20] R. Khatri, M. Charlton, P. Sferlazzo, K. G. Lynn, A. P. Mills Jr., and L. O. Roellig, Appl. Phys. Lett. **57**, 2374, (1990).

[21] J. P. Merrison, M. Charlton, B. I. Deutch, and L. V. Jorgensen, J. Phys: Condens. Matter **4**, L207, (1992).

[22] R. G. Greaves and C. M. Surko, Phys. Rev. Lett. **85**, 1883, (2000).

[23] L. Spitzer, in Physics of Fully Ionised Gas, (Interscience Publishers, New York, 1962), p.585.

[24] C. Amsler *et al.*, Nucl. Instr. and Meth. **A 480** 494 (2002).

[25] R. Brun and F. Rademakers, ROOT - An Object Oriented Data Analysis Framework, Proc. AIHENP '96 Workshop, Lausanne, Sep. 1996, Nucl. Instr. and Meth. in Phys. Res. A **389** 81 (1997). See also http://root.cern.ch/.

[26] CERN Application Software Group, GEANT: Detector Description and Simulation Tool, CERN Program Library W5013, Geneva, 1993. See also http://wwwinfo.cern.ch/asd/geant/

[27] H. Bethe and E. Salpeter, *Quantum Mechanics of One- and Two-Electron Systems*, (Springer, Berlin, Heidelberg, New York, 1957).

[28] A. Müller and A. Wolf, Hyperfine Interact. **109**, 233, (1997).

[29] M. E. Glinsky and T. M. O'Neill, Phys. Fluids B **1279**, (1991).

[30] E .M. Hollmann, F. Andergg and C. F. Driscoll, Physcs. Plasma **7**, 2776, (2000).

[31] R. G. Greaves and C. M. Surko, Physcs. Plasma **8**, 1879, (2001).

[32] F. Andergg, E. M. Hollmann and C. F. Discoll, Phy. Rev. Lett. **81**, 4875, (1998).

[33] X. -P. Huang, F. Andergg, E .M .Hollmann, C. F. Discoll and T. M. O'Neill, Phy. Rev. Lett. **78**, 875, (1997).

[34] X. -P. Huang, J. J. Bollinger T. B. Mitchell and Wayne M. Itano, Phy. Rev. Lett. **80**, 73, (1998).

[35] D. H. E. Dubin, Phys. Rev. Lett. **66**, 2076 (1986).

[36] D. H. E. Dubin, Phys. Fluids B 5, **295** (1993).

[37] R. C. Davidson, Physics of Nonneutral Plasmas (Addison-Wesley, Redwood, 1990).

[38] H. Higaki, Jpn. J. Appl. Phys. **36**, 5300 (1997).

[39] M. D. Tinkle, R. G. Greaves, C. M. Surko, R. L. Spencer, and G. W. Mason, Phys. Rev. Lett. **72**, 352 (1994).

[40] G. Gabrielse, A. Khabbaz, and D. S. Hall, Phys. Rev. Lett. **82**, 3198, (1999).

[41] M. Niering, R. Holzwarth, J. Reichert, P. Pokasov, Th. Udem, M. Weitz, T. W. Hänsch, P. Lemonde, G. Santarelli, M. Abgrall, P. Laurent, C. Salomon and A. Clairon, Phys. Rev. Lett. **84**, 5496, (2000).

[42] M. H. Holtzscheiter and M. Charlton, Rep. Prog. Phys. **62**, 1, (1999).

[43] G. Gabrielse, X. Fei, L. A. Orozco, R. L. Tjoelker, J. Hans, H. Kalinowsky, J. Hass and W. Kells, Phys. Rev. Lett. **62**, 1360, (1989).

[44] G. Gabrielse, D. Phillips and W. Qunit, Phys. Rev. Lett. **74**, 3544, (1995).

[45] D. S. Hall, Ph.D thesis, Harvard University, Cambridge, Massachusetts, 1997.

[46] T. J. Murphy and C. M. Surko, Phys. Rev. A **46**, 5696, (1992).

[47] R. C. Davidson, *An Introduction to the Physics of Nonneutral Plasmas*, 2nd ed. (Addision-Wesley Publishing Company, Reading, Massachusetts, 1989).

[48] M. Amoretti *et al.*, Nature **419**, 456, (2002).